Investigation of strain hardening near grain boundaries of an aluminum oligocrystal: experiments and crystal based finite element method

Eralp Demir[a,b,*], Ivan Gutierrez-Urrutia[c]

[a] *Faculty of Engineering and Natural Sciences, Sabanci University, Tuzla 34956, Istanbul, Turkey*
[b] *Integrated Manufacturing Technology Research and Application Center, Sabanci University, Tuzla 34956, Istanbul, Turkey*
[c] *Research Center for Structural Materials / NIMS, 305-0047 1-2-1 Sengen Tsukuba Ibaraki, Japan*

Abstract

Grain boundary mechanics plays a key role in the strengthening of polycrystals. In this study, deformation of aluminum grains is investigated to better understand the origins of strengthening mechanisms near the grain boundaries. For this reason a sample with nearly columnar structure was prepared and fully characterized by electron back scattered diffraction measurements using the two side surfaces of the sample before loading. The total strain distribution on one surface of the sample is measured during tensile loading using digital image correlation technique. The numerical studies include implementation of crystal based finite-element model to understand origins of grain boundary strengthening using both local phenomenological, local dislocation density based and non-local strain gradient based constitutive laws. The effects of mesh refinement, through thickness discretization, boundary condition, and orientation scatter are investigated. Comparison of experimental and simulated total strain distributions near grain boundaries suggests the existence of strain gradient hardening. For this reason, a novel non-local flux based model is developed and implemented with a consistent time integration scheme. The non-local strain-gradient based model reveals strain distributions that are in better agreement with the experimental results than the local models that are not able to mimic the level of grain boundary strengthening and also the actual strains. The non-local strain gradient based strain hardening law, that does not require a separate definition of grain boundary elements, was successful in capturing the strengthening effect near grain boundaries.

Keywords: crystal based finite-element method, dislocation density based models, oligocrystal, grain boundary behavior, dislocation flux

1. Introduction

The understanding of polycrystalline plasticity is a complex phenomenon that involves different microstructural features such as grain boundaries, crystal defects, second-phase particles, grain morphology and crystallographic texture. The overall mechanical behavior of polycrystals is strongly dependent on the grain size [1], grain morphology [2], texture [3, 4, 5, 6], and grain boundaries [7] as well as temperature [8, 9], strain-rate [10], crystal structure [11], and mechanical boundary conditions [12]. Therefore, vast amount research has been devoted to understand grain boundary mechanics in order to develop models that mimic the physics of grain boundary behavior.

Bi-crystal studies have been used to understand grain boundary mechanics because of their relatively simpler deformation state than that in the grain of a polycrystal aggregate [13]. In general, multiple slip was dominant near the grain boundaries that becomes pronounced as the misorientation between grains increases [14]. Bi-crystal interactions have been experimentally investigated by surface strain mapping techniques such as digital image correlation (DIC) and electron back scattered diffraction (EBSD) [15, 16]. For instance, these

*Corresponding author
Email address: eralpd@sabanciuniv.edu (Eralp Demir)

techniques have revealed significant amount of crystallographic rotations near aluminum bi-crystal interfaces. The greater orientation changes were measured for the grain boundaries with greater misorientations. This effect was attributed to the occurrence of dislocation pile-ups near high-angle grain boundaries and the relative ease in dislocation slip transfer across low-angle grain boundaries [17].

Similarly, oligocrystal studies have revealed heterogeneous distribution of strain among crystals. In most of the oligocrystal studies, grains had columnar structure and, hence, a single sample surface was typically investigated [18, 19, 20, 21]. Interestingly, some studies have characterized the two opposite sample surfaces to understand the influence of three dimensional grain structure on strain hardening [22, 23, 24]. These studies have revealed that the absolute total strain scales with the grain size in the aggregate. This behavior has been attributed to the occurrence of low level constraints imposed by the neighboring grains, and hence the low hardening interactions of a large grain with its neighbors. Recently, several studies have evaluated temperature effects during loading [25, 26] and slip activity at a finer scale [27]. To sum up, the experimental surface examination methods include optical microscopy, electron microscopy, and EBSD to determine grain size, grain morphology, slip plane traces, orientation changes and misorientation; and DIC methods to quantify plastic strains. More recent advancements in orientation measurements allow full 3D non-destructive in-situ characterization of orientations and stresses inside crystals at high energy X-Ray facilities [28, 29].

Oligocrystal experiments have elucidated the importance of grain size, misorientation, and grain boundary plane on deformation behavior [18, 23, 11]. In particular, these studies have revealed that grain boundaries aligned parallel to the loading direction have negligible effect on deformation behavior of grain interiors. They have also shown that the largest through thickness grain within a test gauge carries the largest strain among other grains.

According to Dawson, grain boundary mechanics can be governed by local constitutive models [30]. The compatible deformation of neighboring grains leads to multiple slip in the proximity of boundaries and hence, higher hardening near grain boundaries compared to that in grain interiors [31]. Crystal based finite-element models incorporate grain interactions by enforcement of the equilibrium and compatibility inside each grain and between the neighboring grains. Accordingly, Hirth attributed strain hardening at interfaces to the compatibility requirement between the neighboring crystals [32]. Grain boundary strengthening is already present in crystal based finite-element methods. Accordingly, finite-element models with local constitutive laws could capture this phenomenon in case the grains were represented with enough level of discretization. For this reason, local crystal plasticity models have been commonly used as a finite-element modeling tool [33, 34, 35]. Recent studies have used additional length scale parameters in strain hardening relations to take into account the grain size dependence [36]. Similarly, new homogenization rules have been developed to consider the effect of grain morphology in local models [37]. However, polycrystal behavior was found to be stochastic since mechanical response depends on various factors such as local dislocation density, residual stress and neighborhood properties in addition to crystal orientation and grain size [38].

A different view states that additional strain hardening near grain boundaries has to be accounted using a separate strain hardening term. Dislocation storage, which is necessary to accommodate the strain mismatch between grains, is believed to be the main source of strengthening near grain boundaries [39]. In this approach, the plastic strain mismatch between neighboring grains was expressed in terms of dislocations. The storage of dislocations at grain boundaries, due to the conservation requirement of Burgers vector[1], causes higher strain hardening rate near the interfaces than in the grain interiors. As a result of dislocation storage, dislocations pile up near the grain boundaries. Dislocation pile up leads to a higher local slip resistance for four main reasons. First, the increase in dislocation density leads to the decrease in the mean-free-path of dislocations (directly correlated to strengthening by the Taylor relation [40]). Second, dislocation pile up prevents further slip at primary systems by exerting long range back-stresses to the nearby dislocation sources. Third, dislocation pile-up enforces secondary slip activation at secondary slip systems, and hence increases the strain hardening rate. Fourth, the activation of secondary slip enhances forest-type dislocation interactions near grain boundaries. Therefore, a strain gradient hardening term has been

[1]Conservation law of Burgers vector states that a dislocation line does not vanish inside a crystal.

introduced to account for the strain gradient hardening near grain boundaries in addition to the statistically stored dislocations [41]. On the other hand, softening can also occur near grain boundaries. For example, low angle grain boundaries and high angle grain boundaries may significantly differ in terms of slip multiplicity differences from grain interior to grain boundary vicinity. It may also occur that deformation constrain near grain boundaries reduces multiple slip comparing to that occurring in grain interiors, as observed by recent SEM and AFM studies of slip traces on crystal surfaces of pure aluminum [42, 43]. Several relevant aspects of dislocation strengthening have been implemented into crystal plasticity modelling. These are the following:

Geometrically Necessary Dislocations (GNDs): Non-local models have been developed to compute strain hardening based on strain gradients or slip gradients [44, 45]. In some works [46, 47], GNDs have been considered as separate nodal variables involving separate definition of the special boundary condition for GNDs other than the displacements such as hard boundaries (i.e. grain boundaries) or dislocation fluxes (i.e. free surfaces).

Grain Boundary Dislocations (GBDs): Grain boundary misfit dislocations, i.e. dislocations that accommodate the misorientation between two neighboring grains, were used to calculate initial dislocation densities for the elements that were next to grain boundaries [48, 49, 50]. Therefore, this method requires a separate definition for the finite-elements that are near grain boundaries. Besides, calculations revealed unreasonably high values of GBD densities that were greater than 10^{16} m^{-2} at grain boundaries due to the $1/b^2$ term (b refers to the Burgers vector) that was present in the calculations. GBDs have been implemented into crystal plasticity simulations to analyze the mechanical behavior of grain boundaries.

Dislocation slip transfer: The relative ease of slip transfer has been recently found to be major factor determining grain boundary behavior. This effect is function of grain boundary character and resolved shear stress [17]. In this context, Roters et al. have predicted the experimental total strain distributions in a bi-crystal sample by modeling the grain boundary slip transfer process as a thermally activated dislocation penetration process [51, 52]. Recently, dislocation storage rate at grain boundaries has been estimated by the calculation of crystallographic shear rates of neighboring regions through the analysis of dislocation slip transmission between neighboring grains [53].

Micro force balance: Gurtin has applied balance laws at the microscopic scale to accurately capture grain boundary mechanics [54]. The computational framework consisted of calculation of geometrically necessary dislocations as result of the plastic incompatibility between neighboring grains (i.e. grain boundary Burgers tensor) and application of equilibrium state to the resulting long-range forces at grain boundaries, i.e. micro force balance. This approach has been used in different works with separate definition of boundary conditions for grain boundaries [55, 56]. In particular, recent models have used gradients of equivalent plastic strains [57] or energetic/dissipative parts of the strain gradients [58].

Grain boundary behavior has been extensively studied by bi-crystal or columnar oligocrystal experiments. These samples, due to the large grain size/sample thickness ratio, allow the investigation of grain interaction mechanisms via surface measurements. However, surface measurements do not represent the exact mechanical behavior of a grain in a polycrystal aggregate since the surfaces are traction-free. Therefore, surfaces are expected to behave more relaxed than the interior regions. Furthermore, grains in a bi-crystal or in a oligocrystal are not fully constrained by the neighboring grains as in a polycrystal aggregate [40]. Although sample surfaces do not exactly represent the mechanical behavior of a grain, surface measurements in bi-crystals or columnar polycrystals provide accurate signatures of grain boundary mechanics since the stress states are simpler than those in polycrystalline aggregates. For this reason, we have conducted experiments on an oligocrystal sample to provide further insights into polycrystal mechanics.

In this study, we aim at addressing two major questions of grain-boundary mediated plasticity: First, what are the effects of mechanical boundary conditions, sample geometry, 2D/3D mesh, mesh refinement, and crystal orientation on grain boundary response? Second, is there a need for a strain gradient model to accurately model the grain boundary mechanical behavior?

Important features of this work:

- Investigation of the effect of different local constitutive laws on the grain boundary mechanical behavior by phenomenological, physically-based, and strain gradient hardening constitutive models.

- Development of a novel strain gradient constitutive model based on dislocation fluxes that requires no additional definition of interface elements.
- Comparison of crystal finite-element model results to experimental strain distributions.

In this work, predictions of grain boundary mechanical behavior estimated by a crystal based finite-element method are validated by experimental total strain distributions. In particular, the occurrence of strain gradient hardening as an additional micro-hardening mechanism at grain boundaries is investigated by crystal based finite-element using different constitutive models, namely, local phenomenological, local dislocation density based, and non-local dislocation density based laws. A coarse-grained aluminum sample was prepared, characterized and tested under tension while total strain distribution on one surface was measured by in-situ DIC. Accordingly, the effect of boundary conditions, crystal orientation scatter inside the grains, through-thickness and in-plane mesh refinement on the total strains were investigated. Further, the capabilities of different local constitutive laws are investigated in the context of experimental heterogeneity of the surface strain distributions and grain boundary stiffening.

Paper is outlined as follows. Section 2 explains the experimental procedures and results. Section 3 describes the finite-element model and single crystal constitutive laws that are used in the modeling approach. Sections 5 and 6 present the discussion of the results and conclusions, respectively.

2. Experiments

2.1. Experimental details

An aluminum sample with 99.9 % purity was obtained by rolling a rectangular ingot to 100 % thickness reduction by three rolling passes. The two sides of the ingot were chemically etched with 40 % HNO_3 solution at room temperature to visually observe the grains from both surfaces. The ingot was then annealed at 550 C° for 2 hours until the size of the grains reached few millimeters in size. Inspection of grain size after annealing was performed by optical light microscopy. The gauge location was determined from a region in which the same grains appear on the both side surfaces of the sample. Tensile gauge with dimensions of 3 mm thickness, 5 mm width and 21.7 mm length was cut from the ingot by wire electro discharge machining (WEDM). The test gauge was wet ground and polished with 6 μm, 3 μm and 1 μm diamond paste and with a final solution of 0.1 μm colloidal silica. Slight rounding off the edges was noted after polishing. EBSD measurements were performed on the two opposite surfaces of the test gauge by a JEOL JSM 6490 scanning electron microscope (SEM) at 30 keV with 50 μm step size over the whole sample.

2.2. Experimental results

Figure 1 shows the inverse pole figure maps along the Z-axis before loading. The sample exhibited strong $< 1\,0\,0 > \{0\,0\,1\}$ cube texture as expected for recrystallized aluminum [59]. The equal number of grains on both sides of the sample with the same orientation validates the existence of a nearly columnar grain structure within the sample. Grain boundaries are indicated with line segments in white color. For consistency, the sample coordinate reference (X, Y, Z) is the same reference frame as in the FEM analysis, Figure 1. Table 1 shows the transformed Euler angles (φ_1, Φ, φ_2) in Bunge notation with respect to the sample reference in Figure 1. Euler angles were measured from a rectangular cropped region inside every grain. The size of the selected cropped region was the largest size that accounted for the the average effect of the in-grain statistical orientation distribution. Table 1 shows the values of the Schmid factor and inverse of the Taylor factor for the analyzed grains along the loading direction (X-direction in Figure 1).

In-situ measurement of strains from one side surface of the sample (face A) was performed using a digital image correlation (DIC) method during tensile testing of the sample. This technique is explained in detail in [3]. The sample was strained to a maximum engineering strain of 12.2 % that corresponds to end displacement of 2.65 mm with an initial strain rate of 8.1×10^{-4} 1/s. Tests were performed at constant strain rate by displacement controlled mode. Figure 2 shows the experimental setup used for tensile testing.

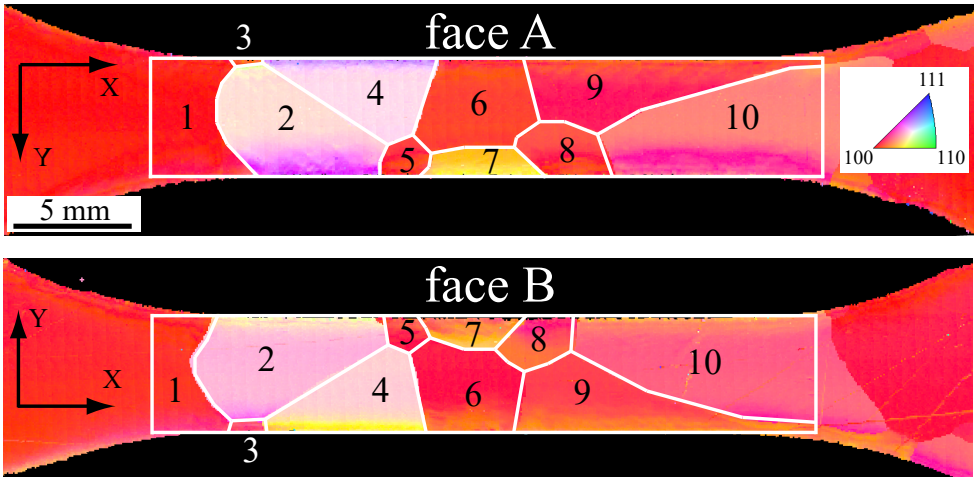

Figure 1: Inverse pole figure maps of both surfaces, i.e. face A and face B, before loading. The sample reference frame is indicated with X, Y, Z directions. The grain boundaries are highlighted with white lines. The color legend corresponding to the crystallographic orientation is shown in the accompanying orientation triangle.

Table 1: Euler angles of the analyzed grains before loading in Bunge convention (φ_1, Φ, φ_2) with respect to the (X, Y, Z) sample coordinate frame that is shown Figure 1.

grain	φ_1 (deg)	Φ (deg)	φ_2 (deg)	Schmid factor	1/Taylor factor
1	161.7	179.1	228.1	0.4934	0.3709
2	357.3	152.0	69.5	0.4918	0.3376
3	286.1	3.2	263.3	0.4643	0.2884
4	31.6	150.6	115.3	0.4858	0.2929
5	113.3	174.7	208.1	0.4371	0.2779
6	350.7	175.3	74.9	0.4457	0.2780
7	285.6	163.0	359.5	0.4507	0.3547
8	104.5	172.5	201.4	0.4474	0.2845
9	344.6	172.9	49.4	0.4962	0.3525
10	7.1	163.8	69.7	0.4944	0.3358

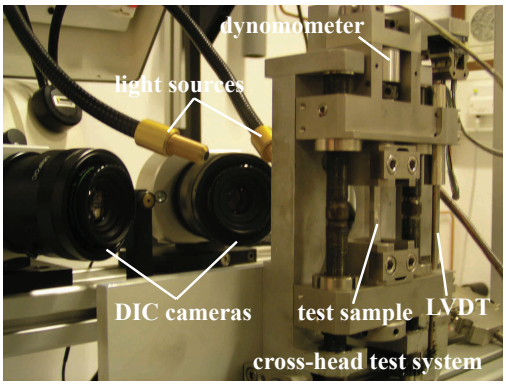

Figure 2: Cross-head test system together with the test gauge, linear variable displacement transducer (LVDT), dynamometer, and digital image correlation (DIC) system.

Figure 3 shows the strain distributions on face A of the sample that are obtained by DIC at 1 %, 5 % and 10 % axial strain levels. The maximum amount of strain is found as 20.5 %, which is higher than the axial 12.2 % engineering strain. This is due to the heterogeneous strain distribution among the grains in the

sample. This effect invalidates the assumption of uniform gauge length under the present testing conditions due to the inhomogeneous nature of strain distributions over the length of the test gauge. For consistency, engineering strain is used as strain indicator in the present work.

Strain measurements revealed the following important observations: **i.** Average strains inside grain-2 and grain-4 exceeded 20 % while average strains inside grain-6 and grain-8 remained roughly at ≈ 2.5 % at the end of loading. **ii.** Strain near the boundary of grain-2 and grain-4 remained approximately an order of magnitude less than that of strains in grain-4 throughout the deformation. **iii.** Strain near the boundary of grain-2 and grain-4 was almost four times less than the strains near the boundary of grain-4 and grain-6.

Table 2: Misorientations, $\theta <$ u v w $>$, between neighboring grains denoted with grain-a and grain-b. Misorientation calculation procedure is shown in appendix D. LAGB and HAGB are the abbreviations used for low- and high-angle grain boundaries, respectively.

grain-a	grain-b	θ (deg)	$<$ u v w $>$	type of GB
1	2	29.4	[0.191 0.397 0.898]	HAGB
1	3	14.5	[0.052 0.186 0.981]	LAGB
2	3	30.5	[0.293 0.360 0.886]	HAGB
2	4	22.5	[0.029 0.685 0.728]	HAGB
2	5	38.6	[0.247 0.601 0.760]	HAGB
4	5	31.6	[0.326 0.386 0.863]	HAGB
4	6	26.0	[0.011 0.532 0.846]	HAGB
5	6	13.9	[0.4097 0.4817 0.7746]	LAGB
5	7	30.4	[0.150 0.676 0.721]	HAGB
6	7	19.0	[0.158 0.571 0.806]	HAGB
6	8	16.6	[0.398 0.481 0.781]	HAGB
6	9	19.6	[0.086 0.094 0.992]	HAGB
7	8	33.5	[0.136 0.677 0.724]	HAGB
8	9	34.8	[0.208 0.303 0.930]	HAGB
8	10	39.8	[0.212 0.426 0.879]	HAGB
9	10	10.2	[0.062 0.178 0.982]	LAGB

Schmid and Taylor factors are calculated by assuming uni-axial stress and strain states, respectively. Schmid factors, shown in Table 1, correlate well with the magnitude of experimental strains in the grains, Figure 3. It exhibits better correspondence to experimental data than those of the inverse of the Taylor factors. The experimental results show that grain-2 and grain-4 deformed to higher strain level than grain-6 and grain-8, which is in good correlation with the calculated Schmid factors. 2-4 grain pair have a lower symmetry in comparison to the other rotated cube grains hence they are expected to deform by single slip. Grain-9, that has the highest Schmid factor, carries a significant amount of the externally applied strain in correlation other grains. However, the strain values do not correlate well with the inverse of the Taylor factors. As expected, this result suggests that in the present oligocrystal work, grains exhibit Sachs-type deformation behavior. In the Taylor approach, applied strain is fully satisfied with minimum slip activation in five of the twelve available slip systems [60], thereby leading to a very strict constraint for a relatively free deforming crystal as the present oligocrystal.

Table 2 reveals that the present oligocrystal does not contain HAGBs with misorientation angle larger than 40°. Most of the analyzed grain boundaries are HAGB. Only three GBs are LAGBs. Grain boundary between grains 9-10 is the boundary with the lowest misorientation angle of the listed GBs (10°) making the 9-10 grain pair as nearly a single grain through the sample width.

Figure 4 shows the EBSD analysis on face B of the sample after deformation to 12.2% tensile strain. White lines indicate {111} slip plane traces. Grain orientation changes slip plane traces inside grain-2 and grain-4, which indicates the occurrence of single or double slip. Shear bands with intense local shear strains were detected in grain-9 and grain-10 by EBSD in correlation with DIC strain maps (Figure 4.a). We found that these shear bands are not aligned along the {111} slip traces. The occurrence of micro shear bands is visible in the photograph of face B of the deformed sample (Figure 4.c). The kernel average misorientation

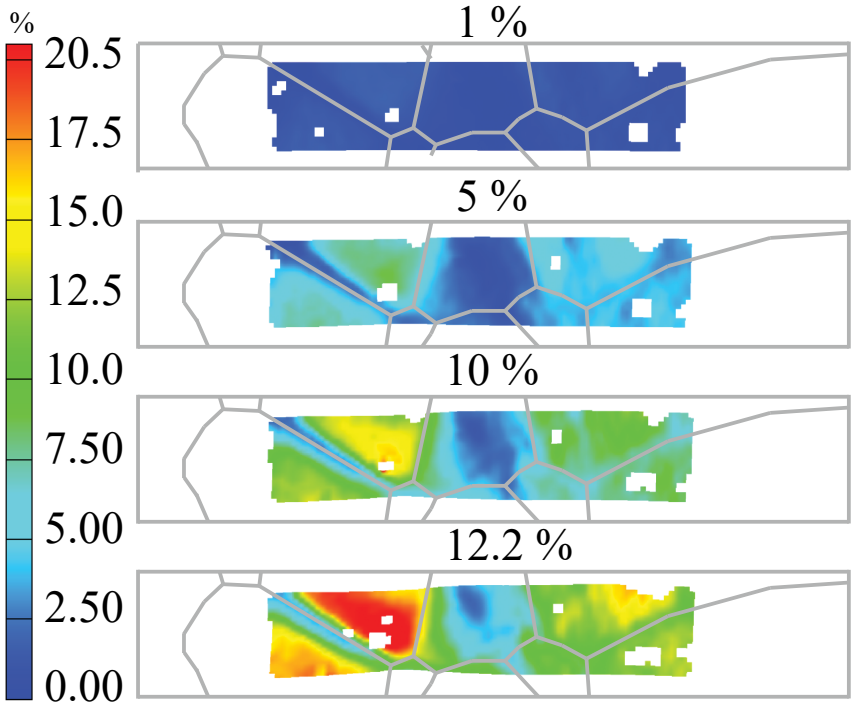

Figure 3: Strain distributions on face A of the sample obtained by digital image correlation (DIC) at 1 %, 5 %, 10 % and 12.2 % tensile strain. Grain boundary between grain-2 and grain-4 is distinctly visible. Sample reference frame is indicated with X, Y, Z directions. White squares indicate the regions without successful measurements.

map[2] (Figure 4.b) shows that the largest misorientation values are detected near the grain boundaries. This result indicates the occurrence of high density of geometrically necessary dislocations around grain boundaries.

Figure 5 plots the change of the areas of individual grains on both faces A and B before straining, and on face B at 12.2% tensile strain. Areal changes indicate the out-of-plane strain that are a fraction of the in-plane strains due to the Poisson effect. The grain area was calculated from EBSD maps by counting the number of pixels per grain using a commercial orientation analysis software. The average difference in grain area between face A and face B, i.e. deviation from columnar structure, was around 11.3 %. Engineering strain was computed from EBSD maps using the change in the grain area by Equation (1) [61]:

$$\epsilon_p \approx \frac{A - A_0}{A_0} \tag{1}$$

Figure 5 reveals that the average strains calculated by this method do not agree with those estimated from DIC. For instance, this approach estimates higher strain level for grain-6 compared to that of grain-4 that does not agree with the strain values obtained by DIC, Figure 3. These results indicate that the estimation of in-grain plastic strain in oligocrystals from the evolving grain areas is inaccurate.

[2]Kernel average misorientation is a measure of the average misorientation between a given data point and its neighbors excluding misorientations higher than some prescribed value.

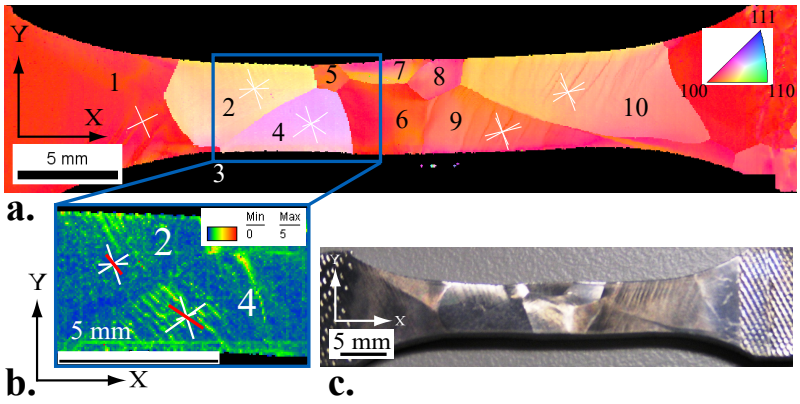

Figure 4: **a.** Inverse pole figure along the Z-axis. Color code is the same as in Figure 1. {111} slip plane traces are indicated with by lines. **b.** Kernel average misorientations (KAM) averaged within first nearest neighbors. {111} Slip plane traces are indicated by white lines. Red lines indicate the active slip systems. **c.** Photograph of face B of the deformed sample to 12.2% tensile strain

.

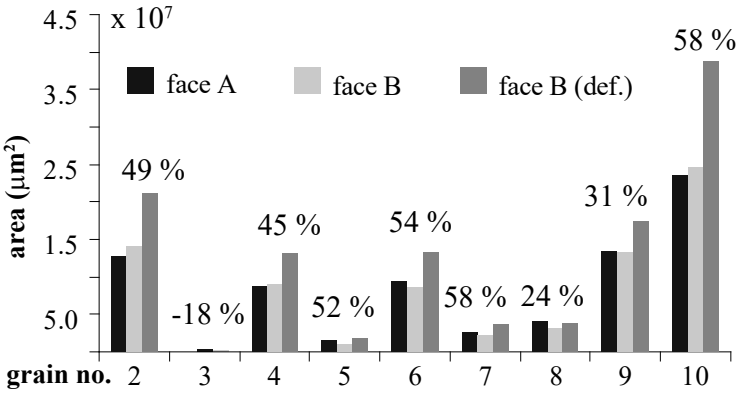

Figure 5: Average grain strain based on the analysis of grain areas determined by EBSD maps. EBSD map of both face A and face B are available before loading and EBSD map of only face B is available at 12.2% tensile strain.

3. Crystal based finite-element model

The proposed model is explained in the following sections. Section 3.1 shows the finite-element method used to obtain the displacement field. Section 3.2 reviews the single crystal deformation kinematics. Section 3.3 shows the constitutive laws used in this work. Section 3.4 explains the method to construct the finite-element model using EBSD maps. Section 3.5 describes the GND based strain gradient hardening model. The time integration procedure for the rate form of constitutive relations is explained in Section 3.6. Section 3.7 shows the mesh and the boundary conditions. Section 3.8 shows the calibration of the model constants. The crystal based finite-element model is implemented in MSC MARC® finite-element software.

3.1. Displacement field iteration

Virtual work principle is applied to a static body at the deformed (spatial) configuration to find the weak form of momentum balance. Equilibrium is enforced weakly in an integral form using Equation (2) over the domain, Ω. In Equation (2), $\mathbf{B}$ is strain-displacement relation (appendix B) for small virtual displacements from equilibrium position, $\mathbf{P}$ is Cauchy stress and $\mathbf{f}$ is externally applied force vector. The domain Ω is

discretized with finite-elements and residual force vector is calculated for each element in the mesh and assembled in usual manner to obtain global residual force vector, $\mathbf{\Psi}$.

$$\mathbf{\Psi} \;=\; \mathbf{f} \;-\; \int_{\Omega} \mathbf{B}^T \,\boldsymbol{\sigma}\, d\Omega \;=\; \mathbf{0} \tag{2}$$

Newton-Raphson (NR) iterative procedure is used to minimize the force residual,$\mathbf{\Psi}$, in Equation (2) for the displacements, $\mathbf{u}_k$. Tangent stiffness matrix, $\mathbf{K_T}$, is needed to perform displacement field iterations as in Equation (3). The subscript k represents the displacement field increment.

$$\mathbf{u}_k \;=\; -\,(\mathbf{K_T})_k^{-1}\,\mathbf{\Psi}_k \tag{3}$$

Position of nodes, $\mathbf{x}_{k+1}$, after $k+1$th iteration is given by Equation (4). NR iteration to find the correct displacement field continues until the norm of the displacement increment, $\|\mathbf{u}\|$, becomes smaller than the prescribed tolerance (10^{-6}).

$$\mathbf{x}_{k+1} \;=\; \mathbf{x}_k \;+\; \mathbf{u}_{k+1} \tag{4}$$

Equation (5) shows the computation of elemental tangent stiffness, $\mathbf{K}_T^{el}$. $\mathbf{K}_T^{el}$ consists of two components; material tangent and geometrical stiffness. Geometric stiffness is calculated using shape function derivatives, $\nabla_{\mathbf{x}}\mathbf{N}$, with respect to the deformed coordinate axes, $\mathbf{x}$ (Appendix A). $\mathbf{K}_T^{el}$ is assembled to obtain global tangent stiffness matrix, $\mathbf{K}_T$.

$$\mathbf{K}_T^{el} \;=\; \int_{\mathrm{V}} \mathbf{B}^T\,\mathbf{D}\,\mathbf{B}\,d\mathrm{v} \;+\; \int_{\mathrm{V}} \nabla_{\mathbf{x}}\mathbf{N}^T\,\boldsymbol{\sigma}\,\nabla_{\mathbf{x}}\mathbf{N}\,d\mathrm{v} \tag{5}$$

Material tangent, $\boldsymbol{\sigma}$, indicates the increment in Cauchy stress, $\boldsymbol{\sigma}$, for an incremental change in the strain, $\partial\boldsymbol{\epsilon}$, from the equilibrium position, Equation (6). Material tangent is calculated using numerical perturbation method as explained in [62].

$$\mathbf{D} \;=\; \frac{\partial\boldsymbol{\sigma}}{\partial\boldsymbol{\epsilon}} \tag{6}$$

The HYPELA2 user subroutine feature of MSC MARC® is used to implement crystal plasticity in a large displacement framework in this study. Finite-element solver gives the deformation gradient, it asks to return the Cauchy stress, $\boldsymbol{\sigma}$, and the material tangent, $\mathbf{D}$. Updated Lagrangian option of the analysis must be selected to use the Cauchy stress as input.

3.2. Crystal plasticity deformation kinematics

Deformation gradient[3], $\mathbf{F}$, is multiplicatively decomposed into its elastic, $\mathbf{F^e}$, and plastic, $\mathbf{F^p}$, parts as in Equation 7. After plastic deformation[4], orientation of a crystal stays the same as its undeformed orientation. Elastic deformation stretches and rotates the ideal plastically deformed crystal lattice.

$$\mathbf{F} = \mathbf{F^e}\,\mathbf{F^p} \tag{7}$$

Green-Lagrange strain is used to calculate the elastic strain, $\mathbf{E^e}$, Equation 8.

$$\mathbf{E^e} = \frac{\mathbf{F^{e}}^T\,\mathbf{F^e} - \mathbf{I}}{2} \tag{8}$$

[3]Capital and small bold letters were used to indicate second and first order tensors, respectively. Letters with regular fonts indicate scalars. $\mathbf{A} : \mathbf{A} = A_{ij}\,A_{ij}$ represents the inner product of a matrix. $\mathbf{I} = \delta_{ij}$ refers to identity matrix or Kronecker delta. || returns the absolute value of a scalar. |||| refers to the norm of a vector or a tensor.

[4]$\mathbf{F^p}$ maps a vector from the undeformed reference configuration to the intermediate configuration (also termed as *relaxed* state since it is the stress free configuration).

Table 3: Slip vectors for an fcc material in the crystal reference frame; $\mathbf{s}_0^\alpha$ and $\mathbf{n}_0^\alpha$ indicate the crystallographic slip direction and slip plane normal of slip system α, respectively.

$\mathbf{n}_0^\alpha$	(111)			$(\bar{1}\bar{1}1)$			$(\bar{1}11)$			$(1\bar{1}1)$		
$\mathbf{s}_0^\alpha$	$[01\bar{1}]$	$[\bar{1}01]$	$[1\bar{1}0]$	$[0\bar{1}\bar{1}]$	$[101]$	$[\bar{1}10]$	$[01\bar{1}]$	$[101]$	$[\bar{1}\bar{1}0]$	$[0\bar{1}\bar{1}]$	$[\bar{1}01]$	$[110]$

$\mathbf{p}$ is the vectorized 2nd Piola-Kirchoff stress that drives dislocation slip at the intermediate configuration. Stress arises due to the elastic stretching of the crystal lattice. In Equation (9), $\mathbf{e^e}$ is the vectorized form of elastic strain and $\mathbf{C}$ is the elasticity matrix at the intermediate configuration.

$$\mathbf{p} \;=\; \mathbf{C}\,\mathbf{e^e} \tag{9}$$

Elastic constants C_{11}, C_{12} and C_{44} are used to construct elasticity matrix at the crystal reference, $\mathbf{C}$. The quantities that belong to crystal reference of each element in the mesh, i.e. $\mathbf{C}$, $\mathbf{s}^\alpha$, $\mathbf{n}^\alpha$ and $\mathbf{S}^\alpha$, are transformed to the sample reference once before the calculations using the transformation in Equation (B.1) at Appendix B.

$$\mathbf{C} \;=\; \begin{bmatrix} C_{11} & C_{12} & C_{12} & 0 & 0 & 0 \\ C_{12} & C_{11} & C_{12} & 0 & 0 & 0 \\ C_{12} & C_{12} & C_{11} & 0 & 0 & 0 \\ 0 & 0 & 0 & 2\,C_{44} & 0 & 0 \\ 0 & 0 & 0 & 0 & 2\,C_{44} & 0 \\ 0 & 0 & 0 & 0 & 0 & 2\,C_{44} \end{bmatrix} \tag{10}$$

Resolved shear stress, τ^α, is the projection of the 2nd P-K stress, $\mathbf{P}$, onto the slip system α with Schmid tensor, $\mathbf{S}^\alpha$. Schmid tensor is obtained by the dyadic product of slip direction and slip plane normal at the intermediate configuration ($\mathbf{S}^\alpha = \mathbf{s}^\alpha \otimes \mathbf{n}^\alpha$). Table 3 shows the twelve slip systems for fcc materials.

$$\tau^\alpha \;=\; \mathbf{F^{eT}}\,\mathbf{F^e}\,\mathbf{P} : \mathbf{S}^\alpha \tag{11}$$

Total amount of plastic shear rate, $\mathbf{L^p}$, refers to the tensorial sum of slip rates, Equation (12).

$$\mathbf{L^p} \;=\; \sum_{\alpha=1}^{12} \mathbf{S}^\alpha\,\dot{\gamma^\alpha} \tag{12}$$

Cauchy stress, $\boldsymbol{\sigma}$, is calculated by the pushing forward 2nd P-K stress to the deformed configuration as in Equation (13).

$$\boldsymbol{\sigma} \;=\; \mathbf{F^e}\,\mathbf{P}\,\mathbf{F^{e}}^{T} \,/\, \det \mathbf{F^e} \tag{13}$$

3.3. Phenomenological constitutive laws

Single-crystal constitutive laws that are known as power law and Voce type strain hardening were used in the present work. The state variable is the critical resolved shear stress per slip system, τ_c^α.

The shear rate on slip systems is calculated using the power law. m is the power of the ratio of resolved shear stress, τ^α, to the critical resolved shear stress, τ_c^α, of the slip system (α). $\dot{\gamma_0^\alpha}$ represents the reference shear rate [63].

$$\dot{\gamma^\alpha} \;=\; \dot{\gamma_0}\,\left|\frac{\tau^\alpha}{\tau_c^\alpha}\right|^{1/m} \mathrm{sgn}(\tau^\alpha) \tag{14}$$

The strain hardening, h^β, of each slip system β, is computed using three different constants, h_0, a, and τ_c^{sat}, which refer to the reference hardening rate, hardening exponent, and saturation value of the

slip resistance, respectively. The hardening exponent gives an additional freedom during calibration of experimental material response.

$$h^{\beta} \;=\; h_0 \,(1 - \frac{\tau_c^{\beta}}{\tau_c^{sat}})^a \tag{15}$$

The strain hardening rate of the slip system α is linearly linked with the slip rates of the other slip systems through the latent hardening matrix, $\mathbf{H}_{\beta}^{\alpha}$. In Equation 17, q is the latent hardening coefficient and $\dot{h^{\beta}}$ is the rate of single-slip system strain hardening.

$$\dot{\tau_c^{\alpha}} \;=\; \textstyle\sum_{\beta=1}^{12} \mathbf{H}^{\alpha\,\beta}\; h^{\beta}\; \left|\dot{\gamma^{\beta}}\right| \tag{16}$$

$$\mathbf{H}^{\alpha\,\beta} \;=\; \begin{bmatrix} \mathbf{1} & q & q & q \\ q & \mathbf{1} & q & q \\ q & q & \mathbf{1} & q \\ q & q & q & \mathbf{1} \end{bmatrix} \tag{17}$$

3.4. Dislocation-density-based constitutive laws

In this section, the crystal plasticity dislocation-density-based constitutive laws are developed. Two different state variables per slip system are defined to account for the evolution of statistically stored dislocations (SSD) as the density of edge type of dislocations, $\varrho_{SSD,e}^{\alpha}$, and the density of screw type of dislocations, $\varrho_{SSD,s}^{\alpha}$, per slip system, α.

The average spacing between the dislocations, l^{α} are both inversely proportional to the square root of the dislocation densities [40] as shown in Equations (18) and (19) for edge and screw dislocations, respectively.

$$l_e^{\alpha} \;=\; \frac{1}{\sqrt{\varrho_{SSD,e}^{\alpha}}} \tag{18}$$

$$l_s^{\alpha} \;=\; \frac{1}{\sqrt{\varrho_{SSD,s}^{\alpha}}} \tag{19}$$

3.4.1. Forest dislocation density

Dislocations piercing through the slip plane are referred to as forest dislocations, ϱ_f^{α}. The forest dislocation density is determined by the projection of the slip plane normal directions of the dislocations, $\mathbf{n}^{\beta}$ onto the slip plane normal, $\mathbf{n}^{\alpha}$, of the desired slip system α as in Equation (20). An interaction matrix, $\boldsymbol{\chi}_{\alpha}^{\beta}$, is used to scale the forest effect of different type of dislocations

$$\varrho_f^{\alpha} \;=\; \sum_{\beta=1}^{12} \boldsymbol{\chi}_{\alpha}^{\beta} \left(\left|\mathbf{n}^{\alpha} \cdot \mathbf{t}^{\beta}\right| \varrho_{SSD,e}^{\beta} \;+\; \left|\mathbf{n}^{\alpha} \cdot \mathbf{s}^{\beta}\right| \varrho_{SSD,s}^{\beta} \right) \tag{20}$$

In Equation (20), $\boldsymbol{\chi}_{\alpha}^{\beta}$ is the dislocation interaction matrix that accounts for the difference in the forest interactions among the slip systems owing to different lock forming mechanisms as applied in the references [45, 64, 65]. The dislocation interaction coefficients $g_0, g_1, g_2, g_3, g_4, g_5$ refer to the self, co-planar, cross-slip, glissile, Hirth lock, and Lomer-Cottrell lock dislocation interactions with values of 1.0, 2.2, 3.0, 3.8, 1.6, and

4.5, respectively [66].

$$\boldsymbol{\chi}_{\beta}^{\alpha} = \begin{bmatrix} g_0 & g_1 & g_1 & g_4 & g_5 & g_3 & g_4 & g_3 & g_5 & g_2 & g_3 & g_3 \\ & g_0 & g_1 & g_5 & g_4 & g_3 & g_3 & g_2 & g_3 & g_3 & g_4 & g_5 \\ & & g_0 & g_3 & g_3 & g_2 & g_5 & g_3 & g_4 & g_3 & g_5 & g_4 \\ & & & g_0 & g_1 & g_1 & g_2 & g_3 & g_3 & g_4 & g_3 & g_5 \\ & & & & g_0 & g_1 & g_3 & g_4 & g_5 & g_3 & g_2 & g_3 \\ & & & & & g_0 & g_3 & g_5 & g_4 & g_5 & g_3 & g_4 \\ & & & & & & g_0 & g_1 & g_1 & g_4 & g_5 & g_3 \\ & & & & & & & g_0 & g_1 & g_5 & g_4 & g_3 \\ & & & & & & & & g_0 & g_3 & g_3 & g_2 \\ & & & & & & & & & g_0 & g_1 & g_1 \\ & & & & & & & & & & g_0 & g_1 \\ & & & & & & & & & & & g_0 \end{bmatrix} \tag{21}$$

Note that the interaction matrix is used to forest density together with the projection operators as in Equation (20). Therefore, directions of edge or screw dislocations with the respect to the slip plane is considered to account for the well-known difference in the interaction coefficients for edge and screw dislocations [67].

The rate form of the Orowan equation, Equation (22), is used to find the shear rates on the slip systems, $\dot{\gamma^{\alpha}}$ in which, b, ϱ_m^{α}, and v^{α} are Burgers vector, mobile dislocation density, and average glide velocity, respectively.

$$\dot{\gamma^{\alpha}} = \varrho_m^{\alpha}\, b\, v^{\alpha}\, \mathrm{sign}\left(\tau^{\alpha}\right) \tag{22}$$

τ_{μ}^{α} is temperature and rate independent (athermal) part of the flow stress [68]. The temperature dependence of τ_{μ}^{α} is only due to the temperature dependence of the shear modulus[5], G. c_1 is the geometric factor used for scaling of the average spacing of the dislocations and $\varrho_{SSD,e}^{\alpha}$ refers to the density of the edge type of dislocations that cause of the long-range stress.

$$\tau_{\mu}^{\alpha} \;=\; c_1\, G\, b\, \sqrt{\varrho_{SSD,e}^{\alpha}} \tag{23}$$

Long-range stress has been attributed to the formation of polarized dislocation structures which contain most edge type of dislocations. The similarity rule that is suggested by Kocks and Mecking [40] is used to relate the density of edge dislocations inside the walls to the size of the size of the sub-grain structure.

3.4.2. Average glide velocity

The dislocation kinetic model is modified to take into account high strain rates. At low strain rates deformation is controlled by thermally activated glide, v_{th}^{α}. However, crystallographic shearing at high strain rates is governed by the viscous drag, v_{dr}^{α}, above strain rates of 10^4 s^{-1}. These dislocation velocities are combined to calculate the slip rate at any strain rate regime [69]:

$$\frac{1}{v^{\alpha}} \;=\; \frac{1}{v_{dr}^{\alpha}} \;+\; \frac{1}{v_{th}^{\alpha}} \tag{24}$$

The drag velocity, v_{dr}^{α}, at high speed is computed using the difference of the long-range stress from the resolved shear stress.

$$v_{dr}^{\alpha} \;=\; \frac{b\;|\tau^{\alpha}|}{B_0} \tag{25}$$

The drag coefficient, B_0, is computed using Equation (26) in which K, T, c_d, v_s and b represent Boltzmann

[5]The shear modulus, G, is calculated from the elastic constants as $G = 2\sqrt{(C_{11} - C_{12})C_{44}/2}$.

constant, temperature, drag constant, shear wave speed, and Burgers vector, respectively.

$$B_0 \;=\; \frac{K\,T\,c_d}{v_s\,b^2} \tag{26}$$

Shear wave speed is calculated using shear modulus, G, and mass density, ρ, using Equation (27).

$$v_s \;=\; \sqrt{G/\rho} \tag{27}$$

Thermally activated glide velocity is computed using Equation (28).

$$v_{th}^{\alpha} \;=\; \nu_0\,d^{\alpha}\,\exp\left(-\frac{\Delta F}{K\,T}\right)\,\exp\left(\frac{|\tau^{\alpha}|\;-\;\tau_{\mu}^{\alpha}}{K\,T}\,V^{\alpha}\right) \tag{28}$$

Jump distance, d^{α}, is the distance that a dislocation travels after a thermal activation event. d^{α} is a multiple of forest spacing [70] as used in Equation (29).

$$d^{\alpha} \;=\; \frac{c_2}{\sqrt{\varrho_f^{\alpha}}} \tag{29}$$

Activation volume, V^{α}, is the thermally effected region in which thermal activation event took place, hence ΔV^{α} is proportional to the jump distance, d^{α}, Equation (30).

$$\Delta V^{\alpha} \;=\; c_3\,b^2\,d^{\alpha} \tag{30}$$

3.4.3. Mobile dislocation density

A log-normal distribution for dislocation segment lengths [71] is adopted to calculate the mobile dislocation density. The mobile dislocation density, ϱ_m^{α}, is calculated as the fraction of the total screw dislocation density, using Equation (31).

$$\varrho_m^{\alpha} \;=\; r^{\alpha}\,\varrho_{SSD,s}^{\alpha} \tag{31}$$

The fraction of mobile dislocations, $r^{\alpha}(\tau^{\alpha},\varrho_f^{\alpha})$, is determined from applied shear stress and forest spacing [72], Equation (32).

$$r^{\alpha}\left(\tau^{\alpha},\varrho_f^{\alpha}\right) = c_7\;(2\pi)^{3/2}\;\frac{|\tau^{\alpha}|^2}{(G\,b)^2}\;\frac{1}{\varrho_f^{\alpha}} \tag{32}$$

3.4.4. Dislocation density evolution (strain hardening)

Mean-free-path storage of dislocations refers to the average distance that a dislocation travels before it gets stored which is inversely proportional to the square root of the dislocation density. c_4 is material specific strain hardening constant. The average distance between the forest dislocations at the slip system α is computed for edge and screw type of statistically stored dislocations (SSD) that are denoted with subscripts e and s, respectively using Equation (33) [40].

$$\left(\dot{\varrho}_{SSD,x}^{\alpha}\right)^{+} \;=\; c_4\,\sqrt{\varrho_{SSD,x}^{\alpha}}\,\frac{\left|\dot{\gamma^{\alpha}}\right|}{b}, \quad x = e,s \tag{33}$$

In the following we analyze the most relevant dislocation mechanisms controlling the dislocation density evolution.

- *Dipole formation* occurs as a results of the mutual stress field of two polar dislocations. Mobile dislocations form these stable dislocation structures to reduce energy in the lattice. The overall dipole

formation rate is computed using Equation (34) [70].

$$\left(\dot{\varrho}^{\alpha}_{SSD,e}\right)^{+} \;=\; \frac{\sqrt{3}\,G\,\varrho^{\alpha}_{m}}{16\,\pi\;(1-\nu)\;\left|\tau^{\alpha}\;-\;\tau^{\alpha}_{\mu}\right|}\;\left|\dot{\gamma^{\alpha}}\right| \tag{34}$$

- *Dislocation climb* is a temperature dependent diffusion controlled annihilation mechanism. The annihilation rate of dislocations is controlled by climb velocity, v^{α}_{climb}, climb distance, d^{α}_{climb}, and the dislocation density, ϱ^{α}_{SSD} as in Equation (35).

$$\left(\dot{\varrho}^{\alpha}_{SSD,e}\right)^{-} \;=\; -\frac{1}{2}\,v^{\alpha}_{climb}\,d^{\alpha}_{climb}\;\left(\varrho^{\alpha}_{SSD,e}\right)^{2}\;\frac{\left|\dot{\gamma^{\alpha}}\right|}{\dot{\gamma^{\alpha}_{0}}} \tag{35}$$

Climb distance is a multiple of Burger's vector.

$$d^{\alpha}_{climb} \;=\; c_5\,b \tag{36}$$

Climb velocity is computed using Equation (37). Ω represents the unit volume of a cube with the size of Burgers vector ($\Omega \approx b^3$).

$$v^{\alpha}_{climb} \;=\; \frac{D_{eff}\,\Omega}{b\,K_B\,T}\;\left|\sigma^{\alpha}\right| \tag{37}$$

In this work, the projection of stress along the slip plane normal is used as the driving force for dislocation climb as in [73] since the normal stress is the driving force for dislocation climb, Equation (38).

$$\sigma^{\alpha} \;=\; \mathbf{n}^{\alpha}\;\cdot\;\mathbf{P}\;\cdot\;\mathbf{n}^{\alpha} \tag{38}$$

The effective diffusion rate is calculated as the some of volumetric, D_v, and core diffusion rates, $a_c\,D_c$, Equation (39).

$$D_{eff} \;=\; D_v\;+\;\varrho^{\alpha}_{SSD,e}\,a_c\,D_c \tag{39}$$

The diffusion terms are computed using the corresponding volume and core diffusion activation energies, Q_v and Q_c, respectively, Equation (40). D_{v0} and $a_c\,D_{c0}$ are the pre-exponential factors, Equation (41).

$$D_v \;=\; D_{v0}\;\exp\left(-\frac{Q_v}{K_B\,T}\right) \tag{40}$$

$$a_c\,D_c \;=\; a_c\,D_{c0}\;\exp\left(-\frac{Q_c}{K_B\,T}\right) \tag{41}$$

- *Cross-slip* refers to the dislocation annihilation reaction between screw dislocations. Two partial dislocations recombine to become a screw perfect dislocation and change its glide plane, respectively before it cross-slips and mutually annihilates with another screw dislocation. The annihilation rate is given by Equation (42):

$$\left(\dot{\varrho}^{\alpha}_{SSD,s}\right)^{-} \;=\; -2\,\frac{\varrho^{\alpha}_{SSD,s}}{w}\,\frac{\nu_0\,b}{w}\,l^{\alpha}_{s}\,P^{\alpha}\,\frac{\left|\dot{\gamma^{\alpha}}\right|}{\dot{\gamma^{\alpha}_{0}}} \tag{42}$$

l^{α}_{s} represents the length of dislocations that are annihilated after a cross-slip event, $\frac{\nu_0\,b}{w}$ is the attempt frequency for the cross-slip events, $\frac{\varrho^{\alpha}_{SSD,s}}{w}$ is the number of locations at which cross-slip events occur,

w is the width of the site that is a multiple of Burgers vector as in Equation (43), c_6 is used as the material dependent scaling constant for the width of the cross-slip site, $\dot{\gamma_0}$ is the reference shear rate.

$$w \,=\, c_6\, b \tag{43}$$

Equation (44) shows the calculation of probability of a cross-slip event, P^α, for slip system α [74].

$$P^\alpha \,=\, \exp\left(-\frac{Q_{cs}}{K_B\, T}\right)\, \sinh\left(\frac{g\left(Q_{cs}, \tau^\alpha\right)}{K_B\, T}\right) \tag{44}$$

In Equation (45), Q_{cs} and X stand for activation energy for cross-slip and stacking fault energy, respectively. A and B are constants and g represents the unit work necessary to overcome thermal barrier by shear force for cross-slip, Equation (46).

$$Q_{cs} \,=\, A\, G\, b^3\, \frac{G\, b}{\chi}\, \left[\ln\left(B\, G\, b\,/\,\chi\right)\right]^{0.5} \tag{45}$$

$$g\left(Q_{cs}, \tau^\alpha\right) \,=\, Q_{cs}\, \left[\ln\left(B\, G\, b\,/\,\chi\right)\right]^{-0.5}\, b\, \left|\tau^\alpha\right|\,/\,X \tag{46}$$

The slip rate must be used as a multiplier of both the cross-slip and climb dislocation density evolution rates, otherwise dislocation density decreases during elastic deformation or even at time increments without any deformation. Therefore, the cross-slip rate is multiplied by slip rate, $\dot{\gamma^\alpha}$, and normalized by a reference shear rate, $\dot{\gamma_0}$.

- *Overall dislocation evolution rates* The multiplication and annihilation rates provide the evolution rate for edge, $\dot{\varrho}^\alpha_{SSD,e}$, and screw, $\dot{\varrho}^\alpha_{SSD,s}$, types of dislocation populations in Equations (47) and (48), respectively. Dislocation density increases due to the mean-free path hardening and dipole formation mechanisms. Dislocation annihilation reactions include the change of glide planes through cross-slip and dislocation climb mechanisms.

$$\dot{\varrho}^\alpha_{SSD,e} \,=\, \frac{c_4}{b}\, \sqrt{\varrho^\alpha_{SSD,e}}\, \left|\dot{\gamma^\alpha}\right| \,+\, \frac{\sqrt{3}\, G\, \varrho^\alpha_m}{16\, \pi\, (1-\nu)\, \left|\tau^\alpha \,-\, \tau^\alpha_\mu\right|}\, \left|\dot{\gamma^\alpha}\right| \,-\, \frac{D_{eff}\, \left(\varrho^\alpha_{SSD,e}\right)^2\, \Omega}{2\, b\, K_B\, T}\, d^\alpha_{climb}\, \left|\sigma^\alpha\right|\, \frac{\left|\dot{\gamma^\alpha}\right|}{\dot{\gamma_0}} \tag{47}$$

$$\dot{\varrho}^\alpha_{SSD,s} \,=\, \frac{c_4}{b}\, \sqrt{\varrho^\alpha_{SSD,s}}\, \left|\dot{\gamma^\alpha}\right| \,-\, \frac{2\, \nu_0}{c_6^2\, b}\, \sqrt{\varrho^\alpha_{SSD,s}}\, P^\alpha\, \frac{\left|\dot{\gamma^\alpha}\right|}{\dot{\gamma_0}} \tag{48}$$

The evolution relations for screw and edge dislocation populations allow modeling of strain hardening/softening reactions based on physical reactions as climb and cross-slip. Different evolution rates are expected for both family of dislocations at different temperatures and strain-rates, thereby allowing physically based modeling of the temperature dependence of strain hardening response of crystals.

3.5. Strain gradient model

Geometrically necessary dislocation (GNDs) densities are computed at each slip system using a non-local calculation procedure from slip gradients.

Equations (49) and (50) have been used to compute the edge and screw dislocation densities that are geometrically necessary to accommodate slip gradients along the slip direction, ($\mathbf{s}^\alpha$), and along the transverse direction, ($\mathbf{t}^\alpha$), respectively [44, 45].

$$b\,\dot{\varrho}^{\alpha}_{GND,e} \;=\; -\nabla\dot{\gamma^{\alpha}}\cdot\mathbf{s}^{\alpha} \qquad (49) \qquad\qquad b\,\dot{\varrho}^{\alpha}_{GND,s} \;=\; \nabla\dot{\gamma^{\alpha}}\cdot\mathbf{t}^{\alpha} \qquad (50)$$

Integrating over the volume, applying change of basis, and re-arranging terms gives Equations (51) and (52).

$$\int_V \dot{\varrho}^{\alpha}_{GND,e}\,\mathrm{d}V \;=\; \int_V \nabla\cdot\left(-\frac{\dot{\gamma^{\alpha}}}{b}\,\mathbf{s}^{\alpha}\right)\mathrm{d}V \qquad (51) \qquad\qquad \int_V \dot{\varrho}^{\alpha}_{GND,s}\,\mathrm{d}V \;=\; \int_V \nabla\cdot\left(\frac{\dot{\gamma^{\alpha}}}{b}\,\mathbf{t}^{\alpha}\right)\mathrm{d}V \qquad (52)$$

Application of divergence theorem is used to convert this volumetric integral into an area integral. Therefore, GND evolution rates can also be computed from the dislocation fluxes, that are area integrals with area normal indicated with $\mathbf{r}$ as shown in Equations (53) and (54) for edge and screw dislocations, respectively. ω^{α} is the transmission factor that represents the fraction of dislocations that pass through the interfaces that accounts for the slip tranmissibility for slip system α.

$$\dot{\varrho}^{\alpha}_{GND,e} \;=\; \frac{\omega^{\alpha}}{V}\int_A -\frac{\dot{\gamma^{\alpha}}}{b}\mathbf{s}^{\alpha}\cdot\mathbf{r}\,\mathrm{d}A \qquad (53) \qquad\qquad \dot{\varrho}^{\alpha}_{GND,s} \;=\; \frac{\omega^{\alpha}}{V}\int_A \frac{\dot{\gamma^{\alpha}}}{b}\mathbf{t}^{\alpha}\cdot\mathbf{r}\,\mathrm{d}A \qquad (54)$$

Calculation of GNDs in the form of volume integral is a simple and computationally efficient method, hence it has been commonly utilized in strain gradient studies. In this study, strain gradients are calculated using dislocation fluxes that are represented by area integrals. The flux method incorporates the effect of the boundaries without requirement for any definition for interface elements. The area, A, over the volume, V, term in evolution Equations (53) and (54) actually provides the length scale for size dependence. Physically this volume represents the region at which strain gradients are homogenized.

The overall GND density is computed using the time integration as shown in Equations (55) and (56).

$$\varrho^{\alpha}_{GND,e} \;=\; \int_0^t \dot{\varrho}^{\alpha}_{GND,e}\,\mathrm{d}t \qquad (55) \qquad\qquad \varrho^{\alpha}_{GND,s} \;=\; \int_0^t \dot{\varrho}^{\alpha}_{GND,s}\,\mathrm{d}t \qquad (56)$$

Grain boundary interfaces are implemented into the model by using the dislocation flux model. Figure 6 shows two neighboring elements that share the same interface. The elements at the two sides of the interface are indicated by letters A and B. $\mathbf{r}$ is the unit surface normal vector. The slip transfer projection is an indicator of the mismatch between the slip plane traces and slip directions two neighboring elements.

The slip transmission, ω, is the multiple of the projection of the slip plane traces with the projection of the slip directions, Equation (57).

$$\omega^{\alpha} \;=\; |\mathbf{s}^{\alpha}_A\cdot\mathbf{s}^{\alpha}_B|\;|(\mathbf{n}^{\alpha}_A\times\mathbf{r})\cdot(\mathbf{n}^{\alpha}_B\times\mathbf{r})| \qquad (57)$$

Misorientation between two neighbors is used to compute the nearest slip directions and slip planes, Equations (58) and (59). Misorientation calculation procedure is briefly explained in Appendix C.

$$\mathbf{s}^{\alpha}_B \;=\; \nabla\mathbf{g}\cdot\mathbf{s}^{\alpha}_A \qquad (58)$$

$$\mathbf{n}^{\alpha}_B \;=\; \nabla\mathbf{g}\cdot\mathbf{n}^{\alpha}_A \qquad (59)$$

The transmission factor is calculated for all of the numerical quadrature points on the element surfaces within the finite-element mesh. This is only calculated at the initialization stage. Therefore, the changes of the misorientation between neighbor elements and area normals during the deformation are neglected.

Figure 7 shows the numerical calculation scheme of GNDs for an element. The non-local numerical calculation steps are as follows:

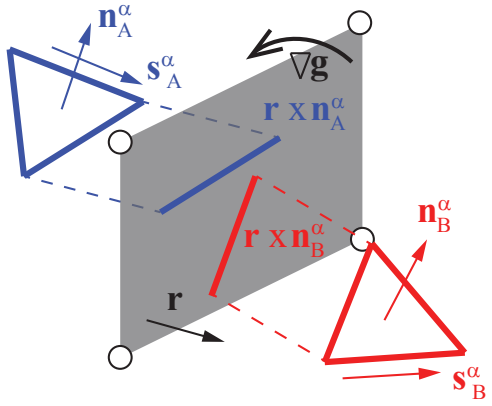

Figure 6: Dislocation fluxes through grain boundaries. Two different grains are represented with the letters A and B. $\mathbf{r}$, $\nabla\mathbf{g}$, $\mathbf{s}^{\alpha}$, and $\mathbf{n}^{\alpha}$ denote the surface interface normal, misorientation between the two grains, slip direction and slip plane normal of the slip system α.

(i) Identification of the convergent values of the slip rates, $\dot{\gamma^{\alpha}}$, at each integration point of each element.

(ii) Extrapolation of slip rates to the nodes using the inverse of the interpolation functions that are computed at the integration points, $\mathbf{N}^{-1}$.

(iii) Calculation of slip rates at the surface quadrature points are computed by surface interpolation functions, $\mathbf{N}_s$.

(iv) Computation of the dislocation fluxes on each of the surfaces using the area integrals shown in Equations (53) and (54) for edge and screw dislocations, respectively.

(v) Calculation of the net dislocation flux by summing up all the surface fluxes.

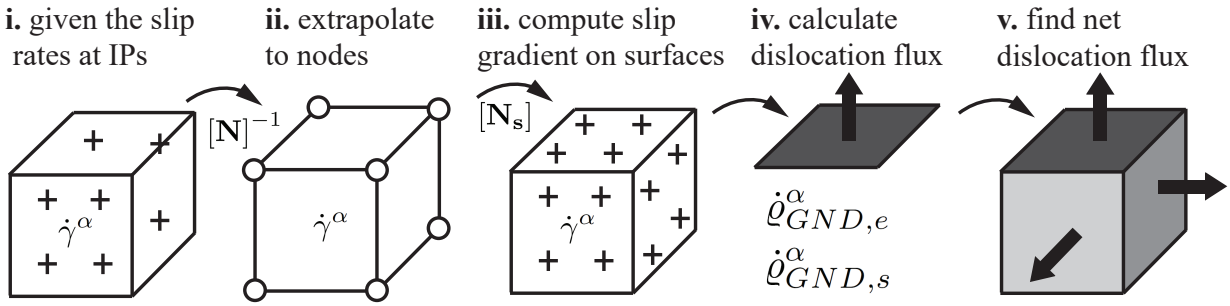

Figure 7: Schematic computation steps for calculation of geometrically necessary dislocation density for a finite-element.

The effect of GNDs on the constitutive behavior are introduced by the modification of the constitutive laws for SSD using the following relations:

- GNDs effect the strain hardening with the mean-spacing relation, l_{α} as in Equations (60) and (61) :

$$l^{\alpha}_{e} = \frac{1}{\sqrt{\varrho^{\alpha}_{SSD,e} + |\varrho^{\alpha}_{GND,e}|}} \tag{60}$$

$$l_s^{\alpha} \;=\; \frac{1}{\sqrt{\varrho_{SSD,s}^{\alpha} \;+\; |\varrho_{GND,s}^{\alpha}|}} \tag{61}$$

- GNDs effect the forest spacing by Equation (62):

$$\varrho_f^{\alpha} \;=\; \sum_{\beta=1}^{12} \boldsymbol{\chi}_{\alpha}^{\beta} \left[\left| \mathbf{n}^{\alpha} \cdot \mathbf{t}^{\beta} \right| \left(\varrho_{SSD,e}^{\beta} \;+\; \left| \varrho_{GND,e}^{\beta} \right| \right) \;+\; \left| \mathbf{n}^{\alpha} \cdot \mathbf{s}^{\beta} \right| \left(\varrho_{SSD,s}^{\beta} \;+\; \left| \varrho_{GND,s}^{\beta} \right| \right) \right] \tag{62}$$

GNDs do not annihilate even at elevated temperatures since they are geometrically necessary and they need to accommodate strain gradients [39]. Therefore, in the current study GND are not considered in the annihilation equations. However, the strain hardening effect of GNDs are considered in the dislocation storage reactions in accordance with Equations (60) and (61).

3.6. Time integration of constitutive laws

At the initialization process, the initial values of the state variables (phenomenological law: τ_c^{α}; local dislocation density based law: $\varrho_{SSD,e}$, $\varrho_{SSD,s}$; non-local dislocation density based law: $\varrho_{SSD,e}$, $\varrho_{SSD,s}$, $\varrho_{GND,e}$, and $\varrho_{GND,s}$) are given. GNDs for all the slip systems, α, are assigned as zero initially, i.e. $(\varrho_{GND,e}^{\alpha})_{t=0} = (\varrho_{GND,s}^{\alpha})_{t=0} = 0$. Similarly, the interfaces are identified for each finite-element and transmission factors at each interface, ω^{α}, is computed at the initialization process once at the beginning.

The time integration method of Dawson-Maniatty is used in this work [75]. An overview of the two level semi-implicit time integration method can be found in [76, 72]. Two level semi-implicit iteration procedure is used for the local constitutive laws and a third level is added for the consistent time integration of non-local constitutive laws.

- At the innermost level, crystal plasticity kinematic equations are integrated. The residual at the current iteration step, $(\mathbf{R})^{[i]}$, is formulated in terms of the plastic part of the deformation gradient, and it is minimized by the Newton-Raphson method in an iterative way. The superscript $[i]$ denotes the ith iteration step in the innermost $\mathbf{F^p}$ loop.

$$(\mathbf{R})^{[i]} \;=\; \sum_{\alpha=1}^{12} \mathbf{S}^{\alpha} \left(\dot{\gamma^{\alpha}} \right)^{[i]} \;-\; \frac{\mathbf{I} \;-\; \mathbf{F^p}_t \left(\mathbf{F^p}^{-1} \right)^{[i]}}{\Delta t} \;+\; \lambda_p \, \det[(\mathbf{F^p})^{[i]}] \, \mathbf{I} \tag{63}$$

The increment of plastic deformation gradient,$(\Delta \mathbf{F^p})^{i}$, is given by:

$$(\Delta \mathbf{F^p})^{[i]} \;=\; -\left[\frac{\partial \, (\mathbf{R})^{[i]}}{\partial \, (\mathbf{F^p})^{[i]}} \right]^{-1} (\mathbf{R})^{[i]} \tag{64}$$

The new plastic deformation gradient at the next iteration, $(\mathbf{F^p})^{[i+1]}$, becomes,

$$(\mathbf{F^p})^{[i+1]} \;=\; (\mathbf{F^p})^{[i]} \;+\; (\Delta \mathbf{F^p})^{[i]} \tag{65}$$

- In the second level of iterations, slip resistivity at the current iteration step, $(\tau_c^{\alpha})^{[l+1]}$, is updated by the Euler time integration method. The superscript $[j]$ denote the jth iteration step in the outer SSD loop.

For the phenomenological constitutive laws, the state variable is the critical resolved shear stress:

$$(\tau_c^{\alpha})^{[j+1]} \;=\; (\tau_c^{\alpha})_t \;+\; (\dot{\tau_c^{\alpha}})^{[j]} \, \Delta t \tag{66}$$

For the dislocation density based constitutive laws, the state variables are the statistical dislocation density terms:

$$\left(\varrho^{\alpha}_{SSD,e}\right)^{[j+1]} \;=\; \left(\varrho^{\alpha}_{SSD,e}\right)_{t} \;+\; \left(\dot{\varrho}^{\alpha}_{SSD,e}\right)^{[j]}\,\Delta t \tag{67}$$

$$\left(\varrho^{\alpha}_{SSD,s}\right)^{[j+1]} \;=\; \left(\varrho^{\alpha}_{SSD,s}\right)_{t} \;+\; \left(\dot{\varrho}^{\alpha}_{SSD,s}\right)^{[j]}\,\Delta t \tag{68}$$

- In the case of non-local calculations, another iteration loop is added on top of the two level iteration scheme. Therefore, three level semi-implicit iterative scheme is used for to consider the effect of GND density, Equations (69) and (70). Superscripts, $[k]$, represent the kth iteration step in the outermost GND loop.

$$\left(\varrho^{\alpha}_{GND,e}\right)^{[k+1]} \;=\; \left(\varrho^{\alpha}_{GND,e}\right)_{t} \;+\; \left(\dot{\varrho}^{\alpha}_{GND,e}\right)^{[k]}\,\Delta t \tag{69}$$

$$\left(\varrho^{\alpha}_{GND,s}\right)^{[k+1]} \;=\; \left(\varrho^{\alpha}_{GND,s}\right)_{t} \;+\; \left(\dot{\varrho}^{\alpha}_{GND,s}\right)^{[k]}\,\Delta t \tag{70}$$

Convergence at each level of iteration scheme was checked with a specified relative tolerance value. The magnitude of the relative tolerance in the simulations was set to 10^{-6}. The state variables for convergence check are $||\mathbf{F^P}||$ in the first (innermost) loop, τ^{α}_{c} for phenomenological constitutive laws, or $\left|\varrho^{\alpha}_{SSD,e}\right|$ and $\left|\varrho^{\alpha}_{SSD,s}\right|$ for dislocation density based constitutive laws in the second (outer) loop, and for strain gradient hardening, $\left|\varrho^{\alpha}_{GND,e}\right|$ and $\left|\varrho^{\alpha}_{GND,s}\right|$ in the third (outermost) loop.

The finite-element software needs the stress and material tangent of each element and each integration point. Deformation is divided into increments and solution at each increment iteratively through cycles. The deformation gradient is saved during a dummy cycle and very large number is assigned to the diagonals of the tangent stiffness matrix ($\mathbf{D}(i,i) = 10^{10}$) to avoid convergence [52]. At the start of the next iteration cycle, the evolution of GNDs are computed using non-local calculations once for all of the integration points simultaneously and updated. In the same cycle, the tangent stiffness matrix, $\mathbf{D}$, and Cauchy stress, $\boldsymbol{\sigma}$ are computed at each integration point. This procedure is followed in order to satisfy the consistency condition to guarantee the state variables such that stress state always remains on the yield surface.

3.7. Mesh and boundary conditions

The 3D mesh for the grains is constructed using EBSD maps of the two faces of the sample, i.e. faces A and B in Figure 1. First, grain boundaries are defined with the same number of line segments on both faces. Second, these line segments are subdivided into 2D quadrilaterals in both faces. Third, corners of quadrilateral elements are connected along the thickness of the sample to build 3D elements by assuming planar grain boundaries. This procedure is schematically illustrated in Figure 8.

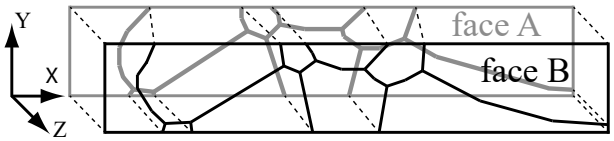

Figure 8: Construction of the 3D mesh for the oligocrystal using EBSD maps. Grain boundaries divided by line segments and the columnar like grain structures are assumed through the thickness.

Finally, elements are refined into smaller elements. 8-node solid brick type of elements are used in all of the simulations. Figure 9 shows the coarse 3D mesh with 1008 number of elements that is used for calibration. Different colors indicate different grains.

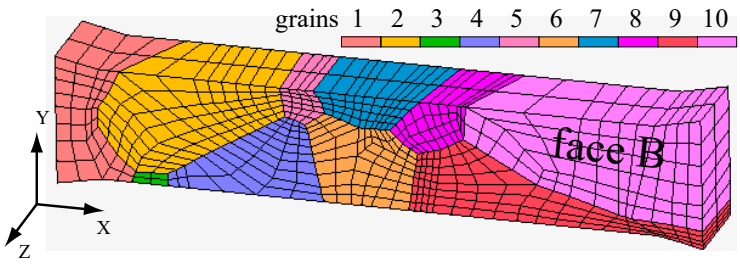

Figure 9: The coarse 3D mesh with 1008 number of elements, boundary conditions and grain orientations that is used for calibration. Different colors indicate different grains. Sample reference frame is indicated by X, Y, Z directions.

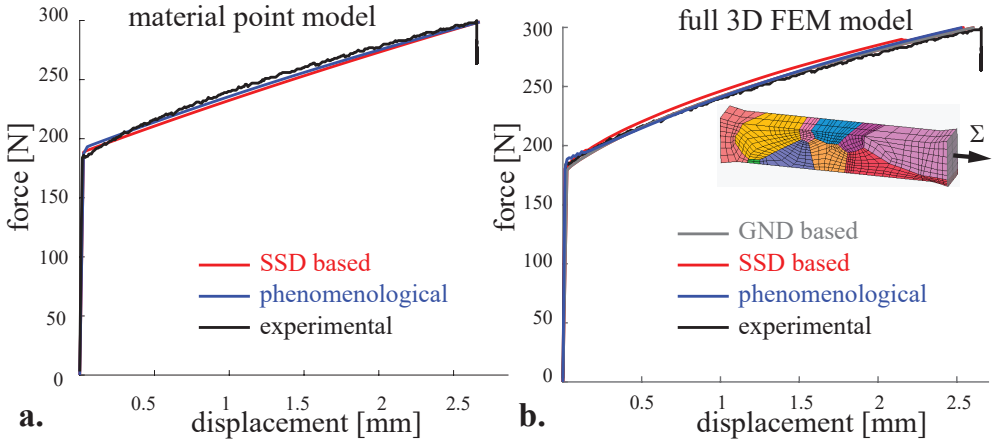

Figure 10: Experimental and simulated force displacement curves after calibration that are obtained by; **a.** material point model, **b.** full 3D FEM model.

3.8. Model constants

Model constants are determined for the best matching experimental and numerical force-displacement response. Calibration is done by two steps. At first, the values for the constants are found iteratively using a material point model in MATLAB® that uses the same constitutive laws as described in this work. A single crystal with cube orientation under tension is used in the material point simulations since the cube texture is dominant in the test sample. At the second step, crystal based finite-element model with the exact measured crystal orientations is used for better calibration. A mesh with 1008 number of elements is used for the calibration of model constants in reasonable computational times. The forces in the simulations are obtained by summing up the nodal reaction forces along X direction at one end of the sample, and subsequent comparison with the experimental force displacement curve. Figure 10 shows the simulation force vs. displacement results for the calibrated curves calculated by the phenomenological, SSD based and GND based models together with the experimental data. The plots show that a resonable match is obtained by the models with the experimental findings using this methodology.

Elastic constants C_{11}, C_{12}, and C_{44} of 106.78, 60.74, and 28.21 GPa, respectively, are used for the present aluminium sample.

Tables 4 and 6 show the values of the calibrated values of the constants used in the phenomenological and dislocation density based models, respectively. Table 5 shows the material constants of the physic based model.

Table 4: Constants used in the phenomenological constitutive laws.

$\dot{\gamma}_0$ (1/s)	m	τ_c^0 (MPa)	h_0 (MPa)	τ_c^{sat} (MPa)	a	q
0.001	0.1	8	36	35	1	1.1

Table 5: Description and values of constants used in the dislocation-density-based constitutive laws[74, 40, 64].

constant	value	unit	description
b	2.86×10^{-10}	m	Burgers vector
K	1.38×10^{-23}	J/K	Boltzmann constant
ΔF	3×10^{-19}	J	Helmholtz free energy for thermal activation
v_D	10^{10}	1/s	Debye frequency of dislocations
A	8×10^{-3}	-	cross-slip constant
B	0.07	-	cross-slip constant
X	200×10^{-3}	J/m^2	stacking fault energy
Q_v	197×10^3	J/mol	volume diffusion activation energy
D_{v0}	2.0×10^{-5}	m^2/s	volume diffusion coefficient
Q_c	117×10^3	J/mol	core diffusion activation energy
$a_c D_{c0}$	1.0×10^{-24}	m^4/s	core diffusion coefficient
ϱ^0	10^{12}	1/m^2	initial dislocation density
$\dot{\gamma_0}$	1.0×10^{-4}	1/s	reference slip rate
ρ	2720	kg/m^3	mass density
c_d	45	-	drag constant

Table 6: Description and values of adjusting parameters in the dislocation density based model.

constant	value	unit	description
c_1	0.12	-	geometric constant for the long range flow stress
c_2	1	-	adjusting parameter for jump distance
c_3	1	-	constant for activation volume
c_4	0.0015	-	mean-free-path hardening constant
c_5	10000	-	adjusting parameter for the width of a cross-slip site
c_6	10	-	multiple for the climb distance
c_7	0.1	-	fraction of mobile dislocation density
c_8	0.1	-	scaling constant for dipole formation

4. Model results

In this section the effects of the boundary conditions, in-plane mesh refinement, through thickness mesh refinement, orientation scatter and type of the constitutive laws on the total strains are investigated.

4.1. Boundary conditions

The effects of three different boundary conditions (BC) on the total strain are investigated. Figure 11 shows the schematic representation of the BCs used in the present simulations. BC-1 represents a free-free boundary condition. Load is applied from the right end as fixed displacements along X direction, since it is a displacement controlled experiment. BC-2 represents a free-free condition together withcross-head motion. To simulate cross-head BC, the nodes at the left end are displaced one half of the total displacement along negative X direction and similarly the nodes at the right end are displaced positively one half of the total displacement along positive X direction. BC-3 shows a fixed-fixed condition while displacements are applied at one end.

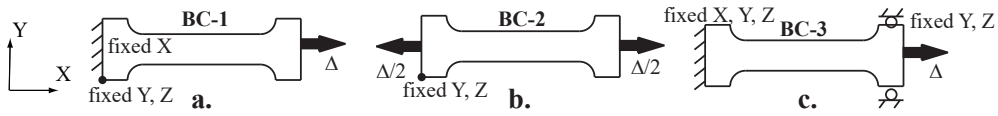

Figure 11: Schematic representation of the Boundary Conditions (BC) used in the simulations: **a.** free-free (BC-1), **b.** free-free with double cross-head (BC-2), and **c.** fixed-fixed (BC-3). The same scale bar as in the strain measurements in Figure 3 is used for consistency.

The comparison of the strain distributions leads to several important conclusions, Figure 12. First, there is little difference between free-free double cross-head motion (BC-1 and BC-2) and free-free BC. Second, fixed-fixed case (BC-3) results in similar strain levels to those attained in the experiments. Free-free boundary conditions are unlikely to be realistic since strains are significantly lower than the experimental observations. Therefore, a fixed-fixed boundary condition (BC-3) is used throughout this study for consistency.

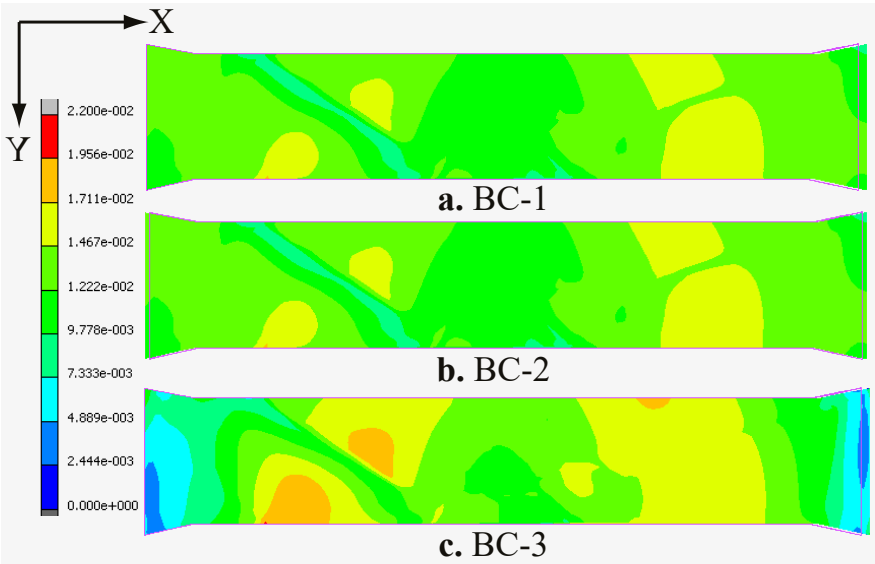

Figure 12: Effect of boundary conditions on the total strain distributions: **a.** free-free (BC-1), **b.** free-free with double cross-head (BC-2), and **c.** fixed-fixed (BC-3). The same scale bar as in the strain measurements shown in Figure 3 is used for consistency.

4.2. 3D grain geometry (through thickness discretization)

The effect of mesh refinement through the thickness sample is investigated using three different mesh refinement levels. For this reason, different mesh types with different (1, 2, 4, and 8) number of elements per thickness are investigated. The aspect ratio of most of the elements remain at a reasonable scale for the thickness division by 4 elements. The total strain becomes indifferent after the mesh refinement level of 4 elements per thickness, hence the results are not shown for simplicity. The refinement level of 4 elements per thickness is used in the rest of the simulations.

4.3. Mesh refinement level (in-plane discretization)

Three different meshes with 4032, 16128 and 64512 number of elements and with two elements through the thickness direction are used to determine the mesh refinement level.

Figure 13 shows the simulated strains on face A of the tensile sample at 1 % axial strain for three different in-plane mesh refinement levels as coarse, moderate, and high (Figure 13 from top to bottom). The strain

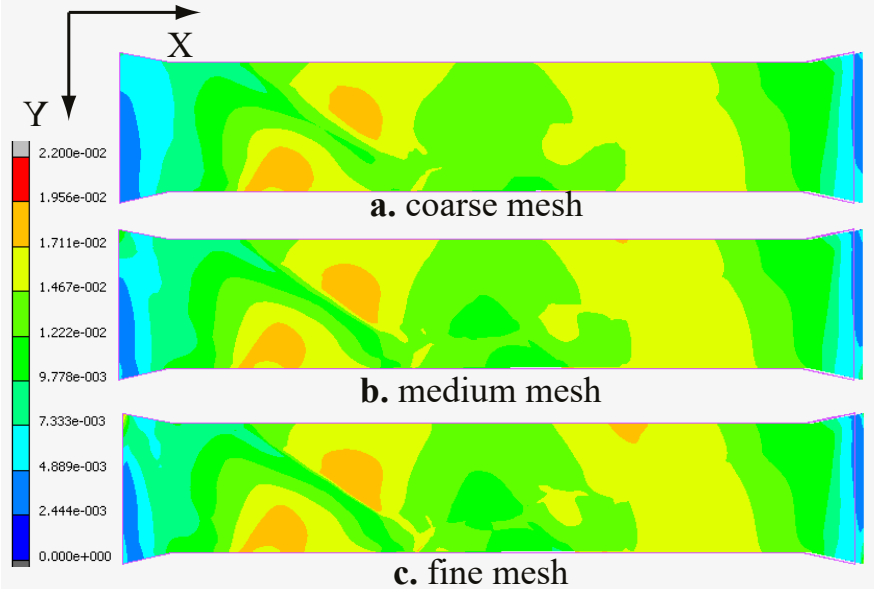

Figure 13: Effect of in-plane mesh refinement on the total strain distributions: **a.** coarse mesh (4031 elements), **b.** medium mesh refinement (16128 elements), and **c.** fine mesh refinement (64512 elements). The same scale bar as in the strain measurements shown in Figure 3 is used for consistency.

distribution of the mesh with medium refinement is similar to that of the fine mesh. The number of elements through the thickness is kept the same to avoid large number of elements. The maximum and the minimum strain values are approximately the same for the moderate and fine meshes. Therefore, moderate mesh refinement with 32256 number of elements is used in the rest of the simulations.

4.4. Orientation scatter

The effect of orientation scatter inside the grains on the strain distribution is investigated. The model uses a single grain orientation per grain. The crystal orientations in Table 1 are obtained by averaging the orientation within a region for each grain. However, it is known that crystal orientation scatter occurs, as revealed by the EBSD crystal orientation measurements. Therefore, there is a need to study the effect of grain orientation scatter on the total strain distributions.

In order to analyze the accuracy of orientation measurement, we have applied a random orientation scatter. Both the magnitude and the direction of the misorientation vector are calculated randomly with a predefined maximum possible magnitude of misorientation angle, similar to [62]. Two different limiting values for the maximum misorientation angles of 5° and 10° are used. The finite-element model with a total of 32256 elements, fixed-fixed boundary conditions (BC-3), four elements per thickness is used for the simulations.

Figure 14 shows the total strain distributions that are obtained by orientations with and without random orientation scatter within the grains. Increasing the misorientation limit of the orientation scatter reduces the magnitude of the maximum total strain and results in a more uniform strain distribution. This is expected since orientation scatter reduces the plastic anisotropy. This study also validates the stability of the selected orientations since the strain level and its distribution among the grains do not change dramatically when a random variation for each element and their integration points was used. For this reason, the orientation scatter is not used in the rest of the simulations, rather a single average crystal orientation is used to represent the crystal orientation of each grain.

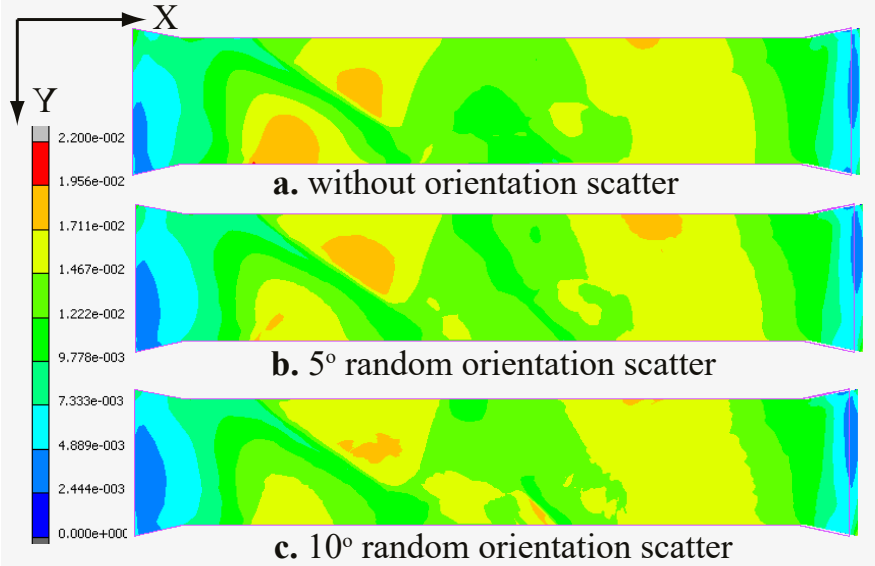

Figure 14: Effect of orientation scatter on the total strain distributions: **a.** without orientation scatter, **b.** 5° orientation scatter, and **c.** 10° orientation scatter. The same scale bar as in the strain measurements shown in Figure 3 is used for consistency.

4.5. Constitutive Laws

In this study, different constitutive laws are implemented and their capabilities on obtaining the resulting anisotropy is quantitatively obtained. Three different constitutive models are used, namely, Phenomenological model, Statistically Stored Dislocation (SSD) density based model, and a Geometrically Necessary Dislocation (GND) density based model based on strain gradients.

Figure 15 shows the strain distributions at 1% axial strain for the experimental and three different models. The phenomenological model captures the general distribution of the total strains however, the experimentally measured strain distribution near the grain boundaries cannot be captured by the phenomenological model. Grain boundary stiffening, that is observed in the experimental strain distributions near grains 2 and 4 shown in Figure 3, cannot be captured by the finite-element simulations using a phenomenological law. For this reason a local SSD model with more physical descriptions is used to explain the experimental strain distributions. The SSD model reveals strain distribution with similar accuracy as the phenomenological model. The strain distributions near the grain boundaries that the SSD model predict agree with the experimental measurements. Therefore a non-local GND model is used to capture grain boundary strengthening accurately. The non-local flux based GND model reveals the best matching strain distribution with the experiments.

The experimental strain curves agree with the simulation results with some distinctly different features. The highest strain level occurs in grain 4 while simulations predict that the highest strain level in grain 2. Similarly, the lowest experimentally measured strain levels in grain 6 is overestimated by the simulations. In addition, the low strain levels near the grain boundary of grains 2 and 4 are overestimated by all of the constitutive models. These findings highlight the deviations from the ideal conditions assumed in the simulations. These deviations stem from differences in grain crystal orientations, deviations from the ideal sample geometry, and/or different surface conditions due to sample preparation (WEDM cutting).

Figure 16 shows the average magnitudes of the state variables at 1% axial strain for three different constitutive laws. The relative magnitudes of the state variables indicates the amount of strain hardening. This figure reveals that the phenomenological model predicts average state variable distribution similar to that predicted by the SSD model. In particular, the phenomenological constitutive law calculates relatively smooth distribution in comparison to the other approaches showing less effect of grain boundaries, Figure 16**a.**. The evolution of SSD density near grain boundaries calculated by the SSD model is significantly

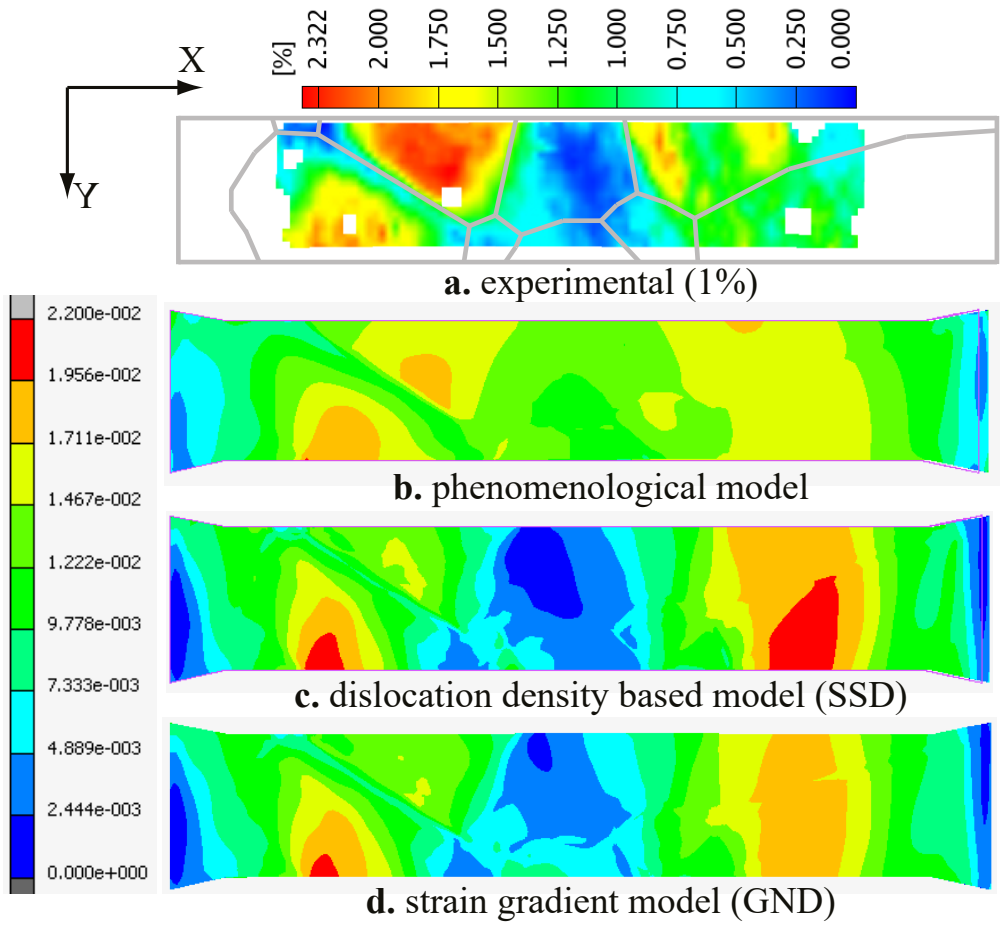

Figure 15: Effects of constitutive laws on the total strain distributions at 1% axial strain: **a.** experimental, **b.** phenomenological model, **c.** dislocation density based (SSD) model, and **d.** non-local dislocation density based (GND) model.

different to that in the grain interiors 16**b.**. On the other hand, the distribution of SSD density calculated by the GND model (Figure 16**c.**), is closer to experimental data. The GND model calculates higher SSD density in grain 2, and lower SSD density near the grain boundary between grain 2 and grain 4, and inside grain 6. Even though GND density is approximately an order of magnitude lower than SSD density, as shown in Figure 16**d.**, a much different evolution of state variables is obtained by the GND model than the SSD model (Figure 16**c.**.) GND densities are highest at the triple junctions. Unexpectedly, GND density is not highest between grains 2-4. This finding indicates the presence of deviations in the modeled geometry of the boundary from the experimental boundary.

5. Discussion

In general, the deformation behavior of the grains in the present coarse grained aluminum sample follow the Schmid/Sachs rule rather than the Taylor type deformation behavior. This is attributed to the relatively free deformation behavior of the grains in an oligocrystal sample in comparison to a polycrystalline aggregate. The grains in the oligocrystal sample tend to deform freely without interacting with neighboring grains unlike to the grains in a polycrystal aggregate. However, relatively stronger constraints are present in a grain in a polycrystalline aggregate due to compatible deformation requirement with its neighbors. In addition, free surfaces behave more relaxed than the interior regions since surfaces are traction-free. Therefore, the

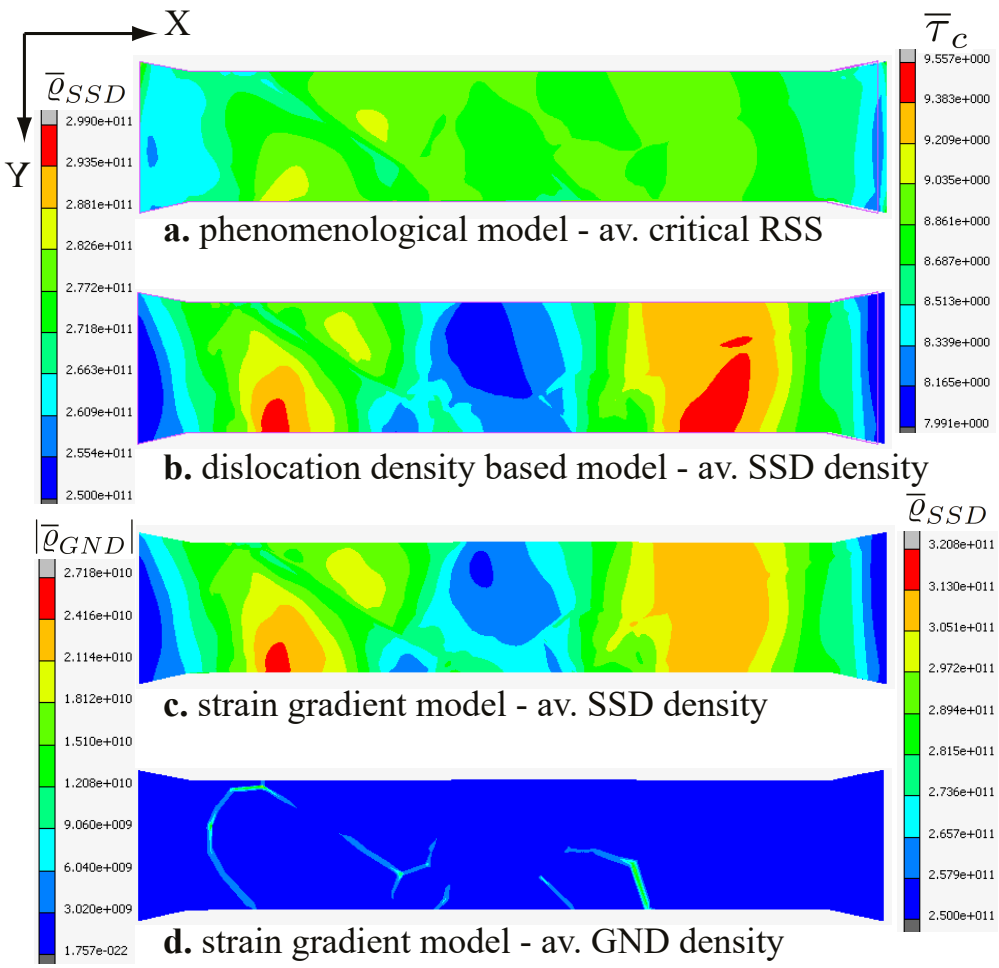

Figure 16: State variables of different constitutive laws at 1% axial strain. **a.** phenomenological model: average critical resolved shear stress (RSS) $\overline{\tau}_c^{\alpha}$, **b.** local dislocation density based model: average SSD density $\overline{\varrho}_{SSD}^{\alpha}$, **c.** non-local dislocation density based model: average SSD density $\overline{\varrho}_{SSD}^{\alpha}$, **d.** non-local dislocation density based model: average GND density $\overline{\varrho}_{GND}^{\alpha}$.

measurements from the free surfaces may reveal different information about the mechanical behavior of a grain. However, in this work grains posses a nearly columnar geometry. Therefore uniform strain field is expected inside the grains along the thickness direction. Accordingly, surface measurements in the present coarse grain material are accurate enough to analyze the strain hardening behavior of the corresponding grains.

Experimental results reveal heterogeneous strain distributions within the grains, as expected. The sample exhibits strong cube texture. However, the amount of applied strain is not uniformly distributed among the grains. Therefore, the strain in each grains is related with the crystal orientation of the grains as well as that grain is constrained by other neighboring grains. For example, the boundary between grain 9 and grain 10 is aligned nearly parallel to the tensile axis, so that it plays no role on the strain partitioning among these grains. However, the boundaries of grain 6 with its neighbors are aligned nearly vertical with respect to the tensile axis. This constrains the deformation of grain 6 with its neighbors, thereby leading to low strain level.

Stiffer grain boundary response is experimentally observed in this study. For example, even though the interiors of grain 2 and grain 4 are strained to the highest strain level in the oligocrystal, the region around their boundary has at least an order magnitude lower strain level than that in the grain interior. 2-4 grain

pair are in single slip zone, Schmid factor in Table 2, which is confirmed to support alone 160% of the overall 12.2% macrostrain. The grain boundary is aligned along the maximum shear stress direction but it exhibits the lowest strain level. This result indicates that the deformation resistance of grain boundary between 2-4 grain pair is low.

The slip resistance of grain boundaries is related to the strain hardening near interfaces due to the storage of dislocations. This can be explained by the experimental strain maps of grains 2, 4 and 6, Figure 3. The misorientation angles between grain 2 and grain 4 and between grain 4 and grain 6 are approximately the same (see Table 2). Strain level within grain 6 is smaller than the strain level inside grain 2, Figure 3. Therefore, plastic strain mismatch is greater between grain 4 and grain 6. This gives rise to higher storage rate of dislocations hence, higher amount of plastic strain gradient hardening near grain 4 and grain 6. On the contrary, experimental strain maps show significant decrease of strain at the boundary between grain 2 and grain 4 while the grain boundary between grain 4 and grain 6 exhibits low strain level, Figure 3. This finding highlights that the grain boundary hardening is not merely function of the strain mismatch between grains, or the amount of misorientation between grains, but also function of grain boundary normal.

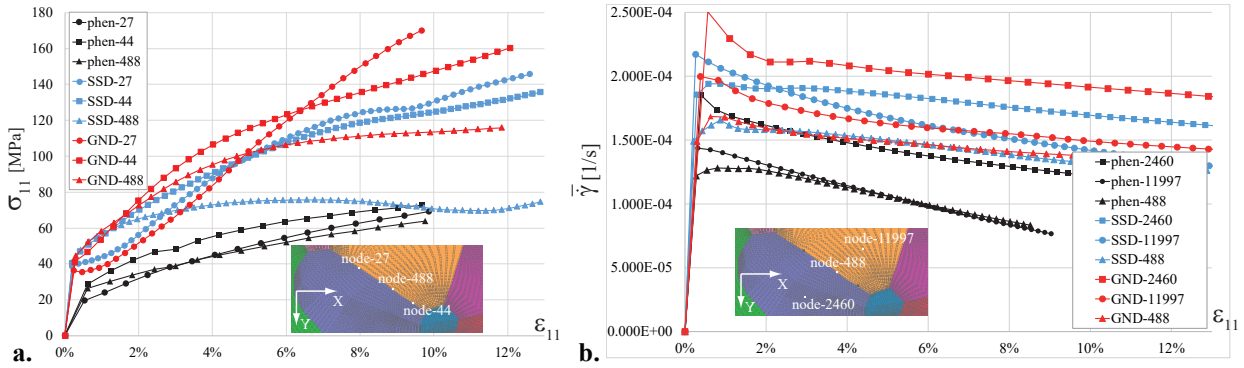

Figure 17: Comparison of **a.** Axial stress (σ_{xx}) vs. axial strain (ϵ_{xx}) and **b.** Average slip rate over the slip systems vs. axial strain (ϵ_{xx}) near boundary of grains 2 and 4. The response of the phenonemenological (phen), dislocation density based (SSD), and geometrically necessary dislocation density based (GND) models are indicated with curves in black, blue, and red colors, respectively.

Figure 17 shows the stress-strain curves that are taken from three different nodes at the boundary between grain 2 and grain 4. The stress-curves in Figure 17.a indicate greater amount of strain hardening for a point closer to a triple junction, as expected. This result indicates that the local finite-element model with phenomenological constitutive laws already incorporates grain interaction effects with strain hardening. However, the stress level near interfaces predicted by the dislocation density based (SSD) model is higher than that predicted by the phenomenological model. The strain hardening rate in the SSD model is initially higher than the phenomenological model followed by some amount of strain softening. The non-local dislocation density based (GND) model however, reveals the highest strain hardening near that boundary among the other model predictions, as expected.

Figure 17.b shows the evolution of average slip activity over axial strain. In all the models, the average slip rates were lowest at the boundary node in comparison to the locations inside the grains suggesting higher slip system activity inside grains than the boundary. GND model reveals the greatest difference between the grain interiors and grain boundary thereby can better capture the grain boundary effects than the other local constitutive models.

The present finite-element model does not take into account in-grain orientation scatter effects, Figure 1. Early studies have shown that a random in-grain orientation scatter leads to strain distributions with less possibility for shear localizations [33], that is in correlation with the experimental findings in [21]. In the present work, the simulations revealed that the in-grain orientation scatter adversely effects the total strain distribution by giving rise to smooth strain distributions with low level of maximum strain.

The crystal based finite-element model was implemented to gain further understanding on the source of strengthening near grain boundaries. For this reason, we first explored a dislocation density based model (SSD model) to take into account the different hardening interactions between dislocations from a physical standpoint. The local dislocation density based model reveals similar response as the phenomenological model.

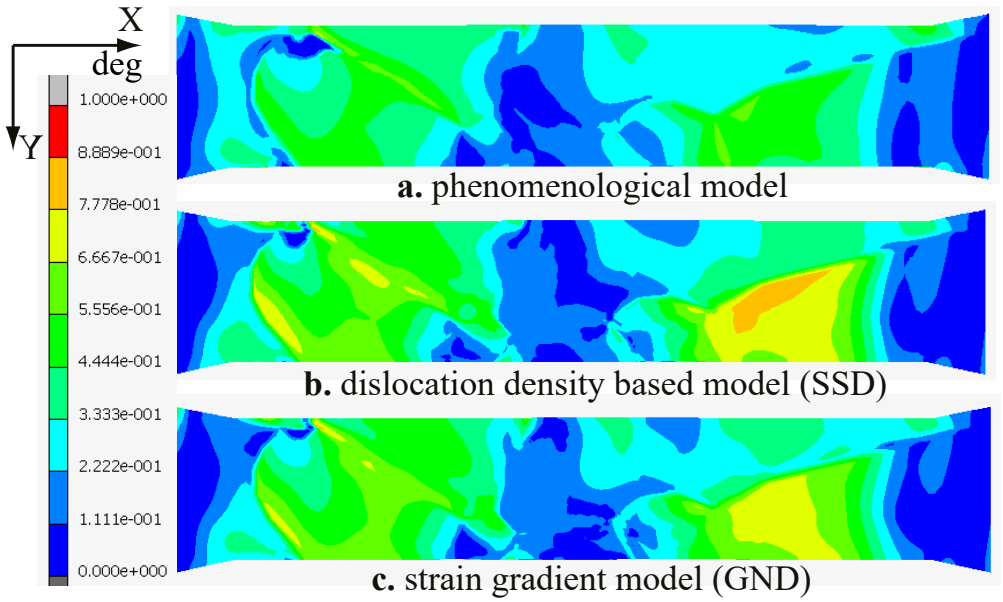

Figure 18: Misorientation distributions in degrees for **a.** phenomenological model, **b.** dislocation density based model (SSD), **c.** strain gradient model (GND).

Figure 18 shows the misorientations that the simulations at 1% axial strain. Misorientation for each element was calculated with respect to the original crystal orientation of that element, Appendix C. Misorientations near the boundaries are higher in comparison to the grain interior for grains 2 and 4. The results of the dislocation density based models are quite different than that of the phenomenological model. This is attributed to the better representation of hardening interactions and dislocation kinematics in dislocation density based models than phenomenological model. However, the difference in the misorientation distribution of GND and SSD models is insignificant. Misorientations are higher in the soft grains (grains 1-2-4-8-9-10) in comparison to the stiff grains (grains 5-6-7). Stiff refers to the higher resistance to plastic flow in this context.

The following question arises: grain boundary hardening occurs as a result of enhanced multiple slip near grain boundaries due to compatibility or is any need to consider any other micro hardening mechanism due to slip gradients? To answer this question we explored a simple flux based strain gradient hardening effect to take into account the grain boundary hardening. The model computes strain gradients using area integrals instead of conventional volumetric integrals of divergence of strain gradients. Therefore, the strain gradient is calculated as a function of misorientation and grain boundary normal between the grains as well as strain mismatch. The strain gradient level is lower than the actual densities for the sub-milimeter sized elements in this oligocrystal case. However, even with small predicted GND densities, the proposed non-local model is in better agreement than both local models. GNDs not only effect strain hardening but also the dislocation kinematics by altering the forest spacing. Grain boundary hardening is not merely function of the strain mismatch between two neighboring grains, but also function of the grain boundary normal and the misorientation between these grains, which is considered in the present model.

6. Conclusions

Experimental conclusions:

- Inhomogeneous strain distributions are measured during the presence of a uniform tensile load. The size relative to the aggregate, geometry and orientation of grains are the main factors effecting the intergranular heterogenity of coarse grained samples.
- The level of hardening near a grain boundary depends on the misorientation, plastic strain mismatch between grains, externally applied stress and grain boundary plane normal.
- The calculation of the average plastic strain of grains using the area of grains as obtained from ex-situ EBSD measurements is not reliable.

Modeling conclusions:

- A local finite-element model is not capable of capturing the strengthening near grain boundaries. Strain gradients and corresponding strain hardening must be incorporated to the model for more accurate representation of the mechanical behavior of grain boundaries.
- A local dislocation density based model (SSD model) that consider the physical hardening interactions between dislocations reveal more realistic mechanical response in comparison to phenomenological models.
- Non-local dislocation density model reveals the nearest strain distributions to the experimental findings.
- Grain boundary stiffening is function of the strain and its difference, misorientation, and grain boundary normal between neighboring grains.
- Dislocation flux based strain gradient hardening provides a simple alternative to incorporate grain boundary/interface effects without requiring any special boundary conditions for interfaces.

7. Acknowledgments

We are grateful to Monika Nellessen for her help with the sample preparation and Herbert Faul for providing the aluminum ingot used in this work. We are also thankful to Dr. Aleksander Kostka for his help on the large scale EBSD measurements. We acknowledge Max-Planck Fellowship to carry out the experimental parts of this research. Corresponding Author (ED) greatly acknowledges the invaluable scientific discussions with Prof. Raabe and Dr. Roters on dislocation fluxes. This project is partly supported by The Scientific and Technological Research Council of Turkey (TUBITAK) under 1001 - Scientific and Technological Research Projects Funding Program with grant no. 118M285.

A. Shape functions and their derivatives

The shape functions of eight-noded solid brick type of elements as a function of the local reference coordinates ξ, η, ζ are as follows.

$$
\begin{aligned}
N_1 &= (1-\xi)(1-\eta)(1+\zeta)/8 \\
N_2 &= (1-\xi)(1-\eta)(1-\zeta)/8 \\
N_3 &= (1-\xi)(1+\eta)(1-\zeta)/8 \\
N_4 &= (1-\xi)(1+\eta)(1+\zeta)/8 \\
N_5 &= (1+\xi)(1-\eta)(1+\zeta)/8 \\
N_6 &= (1+\xi)(1-\eta)(1-\zeta)/8 \\
N_7 &= (1+\xi)(1+\eta)(1-\zeta)/8 \\
N_8 &= (1+\xi)(1+\eta)(1+\zeta)/8
\end{aligned}
$$

Shape function derivatives with respect to the global deformed reference (x, y, z) is given by Equation (A.1) in which $\mathbf{J}$ is the jacobian and N_a is the shape function of node a. $\nabla_{\mathbf{X}} N_a$ in Equation (A.1) represents the shape function derivatives.

$$
\begin{bmatrix} \dfrac{\partial N_a}{\partial x} \\ \dfrac{\partial N_a}{\partial y} \\ \dfrac{\partial N_a}{\partial z} \end{bmatrix} = \mathbf{J}^{-1} \begin{bmatrix} \dfrac{\partial N_a}{\partial \xi} \\ \dfrac{\partial N_a}{\partial \eta} \\ \dfrac{\partial N_a}{\partial \zeta} \end{bmatrix} \tag{A.1}
$$

B. Crystal orientation

Crystal orientation matrix, $\mathbf{g}$, defines the transformation between the crystal and the sample reference frames. $\mathbf{g}$ is computed by Bunge angles $(\varphi_1, \Phi, \varphi_2)$. In (B.1).

$$
\mathbf{g} = \begin{bmatrix} \cos\varphi_1 \cos\varphi_2 - \sin\varphi_1 \sin\varphi_2 \cos\Phi & \sin\varphi_1 \cos\varphi_2 - \cos\varphi_1 \sin\varphi_2 \cos\Phi & \sin\varphi_2 \sin\Phi \\ -\cos\varphi_1 \sin\varphi_2 - \sin\varphi_1 \cos\varphi_2 \cos\Phi & -\sin\varphi_1 \sin\varphi_2 + \cos\varphi_1 \cos\varphi_2 \cos\Phi & \cos\varphi_2 \sin\Phi \\ \sin\varphi_1 \sin\Phi & -\cos\varphi_1 \sin\Phi & \cos\Phi \end{bmatrix} \tag{B.1}
$$

C. Misorientation

Equation (C.1) shows a calculation example of the misorientation, $\nabla\mathbf{g}$, between two grains; grain A and grain B, with crystal orientations of $\mathbf{g}_{(A)}$ and $\mathbf{g}_{(B)}$. 24 cubic crystal symmetry operators, $\mathbf{O}_{(i)}$ (i=1 ... 24), are used to find the minimum net rotation angle between the grains, $\|\nabla\mathbf{g}\|$. Maximum value of misorientation for cubic materials shall not exceed 62.8° due to the symmetry.

$$
\|\nabla\mathbf{g}\| = \min\{\cos^{-1}[\mathrm{tr}(\mathbf{O}_{(i)}\ \mathbf{g}_{(A)}; \mathbf{g}^T_{(B)}\ \mathbf{O}_{(j)})]\} \quad \mathrm{i} = 1\ldots24,\ \mathrm{j} = 1\ldots24 \tag{C.1}
$$

D. Goss compression

Crystal based finite-element model is verified for compression case in which a single crystal is compressed along its [1 1 0] crystallographic axis. The results of the model is shown with 1:1 scale in Figure D.19. A cylinder with a circular cross-section becomes with an elliptical cross-section unlike isotropic material response as expected.

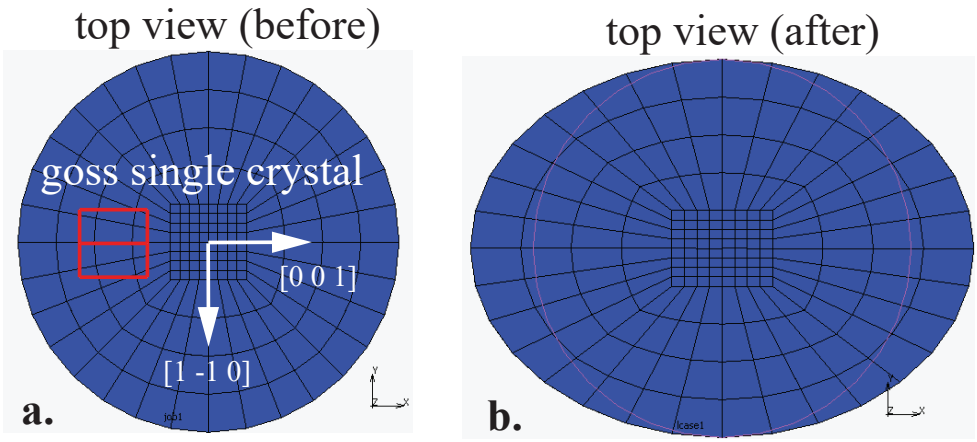

Figure D.19: Goss compression, compression axis is along [1 1 0] crystallographic direction: **a.** top view (initially), **b.** 3D view (initially), and **b.** top view (after 100% compression). The crystallographic directions at the beginning of loading are indicated with white arrows and initial Goss orientation is indicated with a cube in red color.

References

[1] R. Armstrong, I. Codd, R. Douthwaite, N. Petch, The plastic deformation of polycrystalline aggregates, The Philosophical Magazine: A Journal of Theoretical Experimental and Applied Physics 7 (73) (1962) 45–58.

[2] L. Delannay, M. R. Barnett, Modelling the combined effect of grain size and grain shape on plastic anisotropy of metals, International journal of plasticity 32 (2012) 70–84.

[3] M. Sachtleber, Z. Zhao, D. Raabe, Experimental investigation of plastic grain interaction, Materials Science and Engineering: A 336 (1-2) (2002) 81–87.

[4] H. Paul, C. Maurice, J. Driver, Microstructure and microtexture evolution during strain path changes of an initially stable cu single crystal, Acta Materialia 58 (8) (2010) 2799–2813.

[5] A. Godfrey, D. J. Jensen, N. Hansen, Slip pattern, microstructure and local crystallography in an aluminium single crystal of brass orientation {110}¡ 112, Acta materialia 46 (3) (1998) 823–833.

[6] N. Stanford, D. Dunne, M. Ferry, Deformation and annealing of (011)[011] oriented al single crystals, Acta materialia 51 (3) (2003) 665–676.

[7] A. K. Kanjarla, P. Van Houtte, L. Delannay, Assessment of plastic heterogeneity in grain interaction models using crystal plasticity finite element method, International Journal of Plasticity 26 (8) (2010) 1220–1233.

[8] C. Maurice, J. Driver, Hot rolling textures of fcc metals—part i. experimental results on al single and polycrystals, Acta Materialia 45 (11) (1997) 4627–4638.

[9] A. Mecif, B. Bacroix, P. Franciosi, Temperature and orientation dependent plasticity features of cu and al single crystals under axial compression—i. lattice rotation effects and true hardening stages, Acta materialia 45 (1) (1997) 371–381.

[10] A. S. Khan, J. Liu, J. W. Yoon, R. Nambori, Strain rate effect of high purity aluminum single crystals: experiments and simulations, International Journal of Plasticity 67 (2015) 39–52.

[11] X. Tang, L. Peng, S. Shi, M. Fu, Influence of crystal structure on size dependent deformation behavior and strain heterogeneity in micro-scale deformation, International Journal of Plasticity 118 (2019) 147–172.

[12] D. Raabe, M. Sachtleber, Z. Zhao, F. Roters, S. Zaefferer, Micromechanical and macromechanical effects in grain scale polycrystal plasticity experimentation and simulation, Acta Materialia 49 (17) (2001) 3433–3441.

[13] J. Livingston, B. Chalmers, Multiple slip in bicrystal deformation, Acta Metallurgica 5 (6) (1957) 322–327.

[14] Z. Yao, R. Wagoner, Active slip in aluminum multicrystals, Acta metallurgica et materialia 41 (2) (1993) 451–468.

[15] S. Zaefferer, J.-C. Kuo, Z. Zhao, M. Winning, D. Raabe, On the influence of the grain boundary misorientation on the plastic deformation of aluminum bicrystals, Acta Materialia 51 (16) (2003) 4719–4735.

[16] J.-C. Kuo, S. Zaefferer, Z. Zhao, M. Winning, D. Raabe, Deformation behavior of aluminum bicrystals, Advanced Engineering Materials 5 (8) (2003) 563–566.

[17] M. Linne, T. Bieler, S. Daly, The impact of microstructure on the relationship between grain boundary sliding and slip transmission in high purity aluminum, International Journal of Plasticity (2020) 102818.

[18] F. Delaire, J. Raphanel, C. Rey, Plastic heterogeneities of a copper multicrystal deformed in uniaxial tension: experimental study and finite element simulations, Acta Materialia 48 (5) (2000) 1075–1087.

[19] D. Raabe, M. Sachtleber, H. Weiland, G. Scheele, Z. Zhao, Grain-scale micromechanics of polycrystal surfaces during plastic straining, Acta Materialia 51 (6) (2003) 1539–1560.

[20] G. Cailletaud, S. Forest, D. Jeulin, F. Feyel, I. Galliet, V. Mounoury, S. Quilici, Some elements of microstructural mechanics, Computational Materials Science 27 (3) (2003) 351–374.

[21] N. Zhang, W. Tong, An experimental study on grain deformation and interactions in an al-0.5% mg multicrystal, International Journal of Plasticity 20 (3) (2004) 523–542.

[22] A. Bhattacharyya, E. El-Danaf, S. R. Kalidindi, R. D. Doherty, Evolution of grain-scale microstructure during large strain simple compression of polycrystalline aluminum with quasi-columnar grains: Oim measurements and numerical simulations, International Journal of Plasticity 17 (6) (2001) 861–883.

[23] Z. Zhao, M. Ramesh, D. Raabe, A. Cuitino, R. Radovitzky, Investigation of three-dimensional aspects of grain-scale plastic surface deformation of an aluminum oligocrystal, International Journal of Plasticity 24 (12) (2008) 2278–2297.

[24] H. Lim, J. Carroll, C. C. Battaile, T. Buchheit, B. Boyce, C. Weinberger, Grain-scale experimental validation of crystal plasticity finite element simulations of tantalum oligocrystals, International Journal of Plasticity 60 (2014) 1–18.

[25] A. Saai, H. Louche, L. Tabourot, H. Chang, Experimental and numerical study of the thermo-mechanical behavior of al bi-crystal in tension using full field measurements and micromechanical modeling, Mechanics of Materials 42 (3) (2010) 275–292.

[26] C. Badulescu, M. Grédiac, H. Haddadi, J.-D. Mathias, X. Balandraud, H.-S. Tran, Applying the grid method and infrared thermography to investigate plastic deformation in aluminium multicrystal, Mechanics of Materials 43 (1) (2011) 36–53.

[27] A. Guery, F. Hild, F. Latourte, S. Roux, Slip activities in polycrystals determined by coupling dic measurements with crystal plasticity calculations, International Journal of Plasticity 81 (2016) 249–266.

[28] R. Pokharel, J. Lind, S. F. Li, P. Kenesei, R. A. Lebensohn, R. M. Suter, A. D. Rollett, In-situ observation of bulk 3d grain evolution during plastic deformation in polycrystalline cu, International Journal of Plasticity 67 (2015) 217–234.

[29] S. Das, F. Hofmann, E. Tarleton, Consistent determination of geometrically necessary dislocation density from simulations and experiments, International Journal of Plasticity 109 (2018) 18–42.

[30] P. R. Dawson, Computational crystal plasticity, International journal of solids and structures 37 (1-2) (2000) 115–130.

[31] C. Wei, S. Lin, R. Qian, J. Hsiao, Computer simulation of the effect of grain size on the properties of polycrystalline specimens by finite element method, Acta metallurgica et materialia 39 (8) (1991) 2051–2057.

[32] J. P. Hirth, The influence of grain boundaries on mechanical properties, Metallurgical Transactions 3 (12) (1972) 3047–3067.

[33] K.-S. Cheong, E. P. Busso, Effects of lattice misorientations on strain heterogeneities in fcc polycrystals, Journal of the Mechanics and Physics of Solids 54 (4) (2006) 671–689.

[34] Y. Guan, B. Chen, J. Zou, T. B. Britton, J. Jiang, F. P. Dunne, Crystal plasticity modelling and hr-dic measurement of slip activation and strain localization in single and oligo-crystal ni alloys under fatigue, International Journal of Plasticity 88 (2017) 70–88.

[35] P. Baudoin, T. Hama, H. Takuda, Influence of critical resolved shear stress ratios on the response of a commercially pure titanium oligocrystal: crystal plasticity simulations and experiment, International Journal of Plasticity 115 (2019) 111–131.

[36] Y. Aoyagi, T. Tsuru, T. Shimokawa, Crystal plasticity modeling and simulation considering the behavior of the dislocation source of ultrafine-grained metal, International Journal of Plasticity 55 (2014) 43–57.

[37] C. Pinna, Y. Lan, M. Kiu, P. Efthymiadis, M. Lopez-Pedrosa, D. Farrugia, Assessment of crystal plasticity finite element simulations of the hot deformation of metals from local strain and orientation measurements, International Journal of Plasticity 73 24–38.

[38] H. Askari, M. R. Maughan, N. Abdolrahim, D. Sagapuram, D. F. Bahr, H. M. Zbib, A stochastic crystal plasticity framework for deformation of micro-scale polycrystalline materials, International Journal of Plasticity 68 (2015) 21–33.

[39] N. Fleck, G. Muller, M. F. Ashby, J. W. Hutchinson, Strain gradient plasticity: theory and experiment, Acta Metallurgica et materialia 42 (2) (1994) 475–487.

[40] U. Kocks, H. Mecking, Physics and phenomenology of strain hardening: the fcc case, Progress in materials science 48 (3) (2003) 171–273.

[41] H. Lyu, A. Ruimi, H. M. Zbib, A dislocation-based model for deformation and size effect in multi-phase steels, International Journal of Plasticity 72 (2015) 44–59.

[42] B. Beucia, S. Queyreau, C. Kahloun, D. Chaubet, P. Franciosi, B. Bacroix, Plastic strain-induced grain boundary migration (sibm) in pure aluminum: Sem in-situ and afm examinations, International Journal of Plasticity 115 (2019) 29–55.

[43] P. Franciosi, L. Le, G. Monnet, C. Kahloun, M.-H. Chavanne, Investigation of slip system activity in iron at room temperature by sem and afm in-situ tensile and compression tests of iron single crystals, International Journal of Plasticity 65 (2015) 226–249.

[44] E. Busso, F. Meissonnier, N. O'dowd, Gradient-dependent deformation of two-phase single crystals, Journal of the Mechanics and Physics of Solids 48 (11) (2000) 2333–2361.

[45] A. Arsenlis, D. M. Parks, Modeling the evolution of crystallographic dislocation density in crystal plasticity, Journal of the Mechanics and Physics of Solids 50 (9) (2002) 1979–2009.

[46] A. Arsenlis, D. M. Parks, R. Becker, V. V. Bulatov, On the evolution of crystallographic dislocation density in non-homogeneously deforming crystals, Journal of the Mechanics and Physics of Solids 52 (6) (2004) 1213 – 1246.

[47] L. Evers, W. Brekelmans, M. Geers, Non-local crystal plasticity model with intrinsic ssd and gnd effects, Journal of the Mechanics and Physics of Solids 52 (10) (2004) 2379 – 2401.

[48] W. Ashmawi, M. Zikry, Grain boundary effects and void porosity evolution, Mechanics of Materials 35 (3) (2003) 537 – 552.

[49] L. Evers, W. Brekelmans, M. Geers, Scale dependent crystal plasticity framework with dislocation density and grain boundary effects, International Journal of Solids and Structures 41 (18) (2004) 5209 – 5230.

[50] J. Shi, M. Zikry, Grain-boundary interactions and orientation effects on crack behavior in polycrystalline aggregates, International Journal of Solids and Structures 46 (21) (2009) 3914 – 3925.

[51] A. Ma, F. Roters, D. Raabe, On the consideration of interactions between dislocations and grain boundaries in crystal plasticity finite element modeling: Theory, experiments, and simulations, Acta Materialia 54 (8) (2006) 2181 – 2194.

[52] A. Ma, F. Roters, D. Raabe, Studying the effect of grain boundaries in dislocation density based crystal-plasticity finite element simulations, International Journal of Solids and Structures 43 (24) (2006) 7287 – 7303.

[53] P. Shanthraj, P. Eisenlohr, M. Diehl, F. Roters, Numerically robust spectral methods for crystal plasticity simulations of heterogeneous materials, International Journal of Plasticity 66 (2015) 31 – 45, plasticity of Textured Polycrystals In Honor of Prof. Paul Van Houtte.

[54] M. E. Gurtin, A theory of grain boundaries that accounts automatically for grain misorientation and grain-boundary orientation, Journal of the Mechanics and Physics of Solids 56 (2) (2008) 640 – 662.

[55] B. Klusemann, B. Svendsen, H. Vehoff, Modeling and simulation of deformation behavior, orientation gradient development and heterogeneous hardening in thin sheets with coarse texture, International Journal of Plasticity 50 (2013) 109 – 126.

[56] H. Pouriayevali, B.-X. Xu, Decomposition of dislocation densities at grain boundary in a finite-deformation gradient crystal-plasticity framework, International Journal of Plasticity 96 (2017) 36 – 55.

[57] S. Wulfinghoff, E. Bayerschen, T. Böhlke, A gradient plasticity grain boundary yield theory, International Journal of Plasticity 51 (2013) 33 – 46.

[58] E. Bittencourt, On the effects of hardening models and lattice rotations in strain gradient crystal plasticity simulations, International Journal of Plasticity 108 (2018) 169 – 185.

[59] G. E. Totten, D. S. MacKenzie, Handbook of aluminum, Marcel Dekker, 2003.

[60] G. I. TAYLOR, Plastic strain in metals, J. Inst. Metals 62 (1938) 307–324.
URL `https://ci.nii.ac.jp/naid/10026664057/en/`

[61] G. Wu, A. Godfrey, D. J. Jensen, Q. Liu, Deformation strain inhomogeneity in columnar grain nickel, Scripta Materialia 53 (5) (2005) 565 – 570.

[62] S. R. Kalidindi, C. A. Bronkhorst, L. Anand, Crystallographic texture evolution in bulk deformation processing of fcc metals, Journal of the Mechanics and Physics of Solids 40 (3) (1992) 537 – 569.

[63] R. J. Asaro, A. Needleman, Overview no. 42 texture development and strain hardening in rate dependent polycrystals, Acta metallurgica 33 (6) (1985) 923–953.

[64] A. Ma, F. Roters, A constitutive model for fcc single crystals based on dislocation densities and its application to uniaxial compression of aluminium single crystals, Acta Materialia 52 (12) (2004) 3603 – 3612.

[65] M. Lee, H. Lim, B. Adams, J. Hirth, R. Wagoner, A dislocation density-based single crystal constitutive equation, International Journal of Plasticity 26 (7) (2010) 925 – 938.

[66] P. Franciosi, A. Zaoui, Multislip in f.c.c. crystals a theoretical approach compared with experimental data, Acta Metallurgica 30 (8) (1982) 1627 – 1637.

[67] L. Kubin, B. Devincre, T. Hoc, Modeling dislocation storage rates and mean free paths in face-centered cubic crystals, Acta materialia 56 (20) (2008) 6040–6049.

[68] H. Mughrabi, Dislocation wall and cell structures and long-range internal stresses in deformed metal crystals, Acta Metallurgica 31 (9) (1983) 1367 – 1379.

[69] R. A. Austin, D. L. McDowell, A dislocation-based constitutive model for viscoplastic deformation of fcc metals at very high strain rates, International Journal of Plasticity 27 (1) (2011) 1 – 24.

[70] F. Roters, D. Raabe, G. Gottstein, Work hardening in heterogeneous alloys: a microstructural approach based on three internal state variables, Acta Materialia 48 (17) (2000) 4181 – 4189.

[71] G. Gottstein, A. Argon, Dislocation theory of steady state deformation and its approach in creep and dynamic tests, Acta Metallurgica 35 (6) (1987) 1261 – 1271.

[72] E. Demir, A physically based constitutive model for FCC single crystals with a single state variable per slip system, Modelling and Simulation in Materials Science and Engineering 25 (1) (2016) 015009.

[73] M. Geers, M. Cottura, B. Appolaire, E. Busso, S. Forest, A. Villani, Coupled glide-climb diffusion-enhanced crystal plasticity, Journal of the Mechanics and Physics of Solids 70 (2014) 136 – 153.

[74] J. Bonneville, B. Escaig, Cross-slipping process and the stress-orientation dependence in pure copper, Acta Metallurgica 27 (9) (1979) 1477 – 1486.

[75] A. M. Maniatty, P. R. Dawson, Y. S. Lee, A time integration algorithm for elasto-viscoplastic cubic crystals applied to modelling polycrystalline deformation, International Journal for Numerical Methods in Engineering 35 (8) (1992) 1565–1588.

[76] E. Demir, F. Roters, D. Raabe, Bending of single crystal microcantilever beams of cube orientation: Finite element model and experiments, Journal of the Mechanics and Physics of Solids 58 (10) (2010) 1599 – 1612.